Journal of Materials Research and Technology 42 (2026) 3685–3701

Contents lists available at ScienceDirect

Journal of Materials Research and Technology

journal homepage: www.elsevier.com/locate/jmrt

Influence of heat treatment and ECAP on the mechanical properties, microstructure, and corrosion behaviour of a micro alloyed magnesium

Adarsh Rai [a,*], Gaetano Palumbo [b], Szymon Bajda [a], Michal Krzyzanowski [a,c,**], Krystian Sokołowski [d], Jakub Kawałko [d], Paulina Lisiecka-Graca [a], Piotr Bała [a], Björn Wiese [e]

[a] Faculty of Metals Engineering and Industrial Computer Science, AGH University of Krakow, Mickiewicza 30, Krakow, 30-059, Poland
[b] Faculty of Foundry Engineering, AGH University of Krakow, Mickiewicza 30, PL-30059 Krakow, Poland
[c] Birmingham City University, Millennium Point, Curzon Street, Birmingham, B4 7XG, UK
[d] Academic Centre for Materials and Nanotechnology, AGH University of Krakow, 30-059 Krakow, Poland
[e] Materials Technology and Innovation, Institute of Metallic Biomaterials, Helmholtz-Zentrum Hereon, Max-Planck-Straße 1, Geesthacht 21502, Germany

ARTICLE INFO

Keywords:
Magnesium alloy
Grain refinement
Corrosion resistance
Strengthening
Finite element analysis

ABSTRACT

This work explores Mg-Zn-Ca material, with novel grain size achieved through equal channel angular pressing (ECAP). Experimental studies indicate that the mechanical properties of the ECAP-treated alloy have been significantly improved compared to those of the initial alloys. Finite element analysis (FEA) was employed to simulate the process, confirming that the characteristic high-shear-strain bands responsible for grain refinement were successfully induced. The formation of MgCaSi and $Ca_2Mg_6Zn_3$ phases helped to improve the corrosion resistance behaviour of both heat-treated and ECAP-processed alloys. While its overall corrosion resistance was similar to that of the heat-treated alloy, the ECAP-processed alloy showed enhanced resistance to pitting corrosion. This improvement is due to a more uniform protective layer as corrosion product, microstructure homogenization, and finer grains produced during the ECAP process. The protective layers in phosphate-buffered saline (PBS) solution, primarily consisting of phosphates and carbonates, were analyzed using X-ray photoelectron spectroscopy (XPS). These findings suggest that the Mg-Zn-Ca alloy processed by ECAP is a promising candidate for biomedical application due to its superior mechanical and corrosion-resistant properties.

1. Introduction

Traditional metallic biomaterials, such as titanium alloys, cobalt-based alloys, and stainless steels, are widely utilized in load-bearing orthopedic applications due to their robust mechanical strength and fatigue resistance [1–3]. However, these traditional implants present notable clinical drawbacks; their non-degradable nature necessitates secondary surgical procedures for implant removal, while long-term implantation risks the release of toxic metal ions into surrounding tissues [4–6]. To address these critical issues, magnesium-based materials have recently emerged as highly promising bioresorbable alternatives [7,8]. Because Mg-based implants safely degrade in vivo, they eliminate the need for subsequent extractions, significantly reducing both patient stress and healthcare expenses [9–11].

Recently, the utilization of magnesium and its alloys has been preferred for orthopedic implants in comparison to degradable and permanent polymers, permanent ceramics and other permanent metals. Its low density, combined with an elastic modulus close to that of natural bone, reduces stress shielding and mechanical mismatch, which supports better physiological load transfer and implant integration [12,13]. Another major advantage of magnesium is that it is an essential element in the human body, where it supports key metabolic processes. Consequently, its degradation products are well tolerated and can be safely metabolized or excreted, enhancing overall biocompatibility [14]. However, magnesium alloys, when used as biomaterials, have several shortcomings. Biodegradable medical devices require sustained structural integrity throughout the tissue regeneration phase. Unfortunately, magnesium's susceptibility to rapid corrosion often compromises the implant's load-bearing capacity before the recovery is finalized [15]. The high susceptibility to pitting corrosion and rapid degradation of magnesium can be attributed to its low standard electrode potential [16–19]. Furthermore, a critical byproduct of this corrosion process is

* Corresponding author.
** Corresponding author. Faculty of Metals Engineering and Industrial Computer Science, AGH University of Krakow, Mickiewicza 30, Krakow, 30-059, Poland.
E-mail addresses: rai@agh.edu.pl (A. Rai), Michal.Krzyzanowski@bcu.ac.uk (M. Krzyzanowski).

https://doi.org/10.1016/j.jmrt.2026.04.025
Received 6 February 2026; Received in revised form 30 March 2026; Accepted 3 April 2026
Available online 5 April 2026

the rapid evolution of hydrogen gas, and the accumulation of H_2 in the body can lead to serious clinical problems. To prevent the risks of subcutaneous emphysema and localized pH elevation, hydrogen must be discharged in a timely manner [16,17]. Therefore, it is crucial to design a magnesium material that exhibits low and homogeneous degradation while retaining its mechanical integrity throughout the healing process to enhance its service life in the human body.

Several methods were used to improve the corrosion resistance and biocompatibility of Mg and its alloys [20–27]. Recent advancements have shifted attention towards innovative severe plastic deformation methods, including high-pressure torsion, equal channel angular pressing (ECAP), accumulative roll bonding, hard-plate rolling, and asymmetric cross-rolling. These techniques aim to produce Mg materials with ultra-fine grain structures, leading to an exceptional balance of strength, degradability and ductility [28–30]. However, the degradability of Mg-alloys depends significantly on the MgO layer; the stronger and more stable MgO layer acts as a barrier against a corrosive environment [31]. The effectiveness of this layer is affected by various microstructural parameters, such as grain size, phase distribution, presence of alloying elements and the composition of the surrounding medium. Several studies reported that grain refinement can influence corrosion resistance, as finer grain can create a more homogeneous and compact passivation layer compared to coarser grain [32–34]. One of the most well-known methods for producing significantly finer grains is ECAP [35]. This process introduces a severe amount of plastic strain, which leads to substantial grain refinement and a subsequent increase in material strength, as described by the Hall-Petch relationship [36]. This strengthening is beneficial for improving fatigue performance, as the introduction of dislocations during ECAP processing enhances material strength. Fine-grained areas exhibit superior mechanical properties and typically demonstrate better corrosion resistance. However, it is important to note that these fine-grained materials may also be more susceptible to the initiation of corrosion processes. This susceptibility arises from galvanic corrosion effects, where coarse-grained areas, possessing a higher corrosion potential, can accelerate corrosion in the adjacent fine-grained regions. Additionally, dislocation density plays a critical role in corrosion behavior. Regions with higher dislocation density become anodic relative to those with lower density which can reduce overall corrosion resistance [37]. The presence and distribution of secondary phase particles also significantly affect corrosion. For instance, $MgZn_2$ acts as cathodes relative to the anodic magnesium matrix, this galvanic coupling accelerates the breakdown of the matrix immediately surrounding the phase interface [38,39]. Overall, both microstructural features and phase distribution are critical in determining the degradation of magnesium alloys.

To address these limitations, the authors synthesized a micro-alloyed magnesium alloy, novel grain size achieved through the grain refinement of the heat-treated alloy through ECAP. A comprehensive microstructural study comparing ECAP and Mg-alloy was conducted to examine the influence of microstructure on the corrosion resistance and biodegradability of magnesium alloys. Mechanical tests were conducted to investigate the mechanical behavior and performance characteristics of the material. A three-dimensional finite element model of a single ECAP pass was developed in Abaqus/Explicit to simulate the deformation behavior of the alloy at elevated temperatures. Additionally, the time-dependent corrosion behavior was analyzed to investigate the relationship between grain size, alloying elements, and corrosion over time in both ECAP-processed and magnesium (Mg) materials. Chemical analyses were also performed to identify the corrosion products, which are essential for understanding the alloy's biocompatibility.

2. Materials and methods

2.1. Alloy preparation

As shown in Fig. 1, the experimental alloy was synthesized via the direct-chill casting technique, utilizing high-purity elemental precursors: Mg 99.95 wt% (Magnesium Elektron Ltd., UK), Zn 99.99 wt% (Wilhelm Grillo Handelsgesellschaft mbH, Germany), and Ca 99.51 wt% (Alfa Aesar GmbH & Co KG, Germany). During the process, the molten mixture was maintained at a temperature of 720 °C in an Ar-SF_6 protective environment before being cast into steel molds for the permanent direct chill casting method. The alloy melt was subsequently poured into boron nitride-coated steel molds, which were pre-heated to 680 °C. Rapid solidification was achieved through water quenching, resulting in 180 mm long and 65 mm diameter cylindrical casting ingots. To homogenize the microstructure, the as-cast ingots underwent solution annealing at 450 °C for 16 h followed by a water quench at room temperature. Inductively coupled plasma-optical emission spectroscopy (ICP-OES) and spark-optical emission spectroscopy (S-OES) were employed to verify the elemental composition. Because both techniques yielded highly consistent results, only the ICP-OES data are presented in

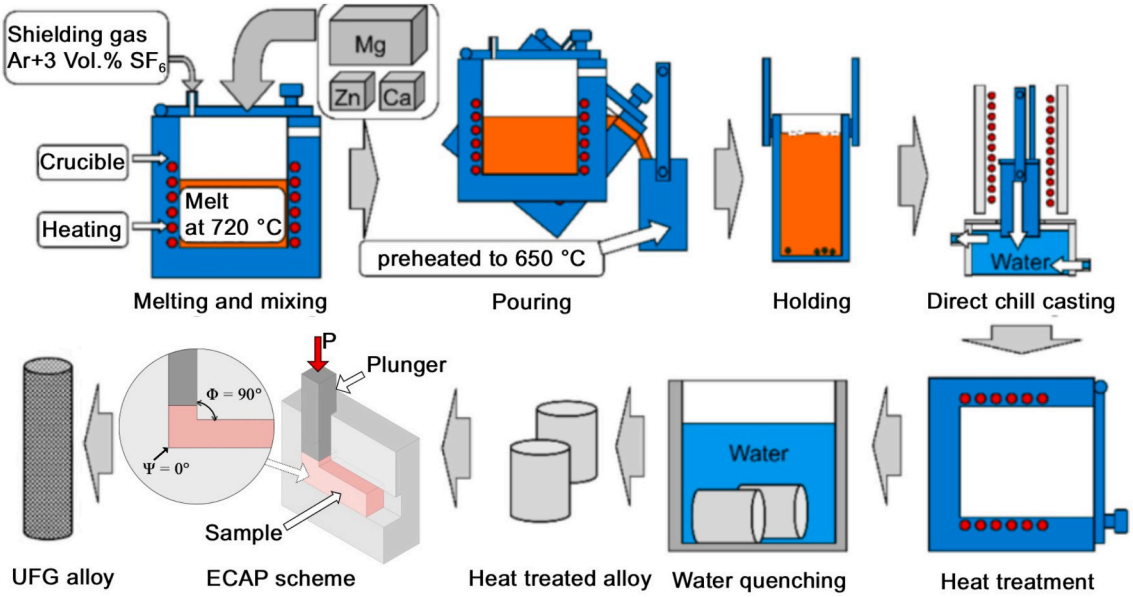

Fig. 1. Mg-0.52Zn-0.23Ca alloy production flow diagram.

Table 1
Chemical composition of studied Mg-alloy.

Element	(wt. %)
Zn	0.52 ± 0.02
Ca	0.23 ± 0.02
Mn	0.0213 ± 0.0005
Si	0.0185 ± 0.0004
Al	0.0043 ± 0.0005
Fe	0.0023 ± 0.0006
Cu	<0.0003
Ni	<0.0003
Be	<0.0003
Mg	Bal.

Table 1. The presence of Si has been detected around 180 ppm; it might come from raw material during casting process.

2.2. Equal channel angular pressing (ECAP)

Wire Electrical Discharge Machining (WEDM) (using a Mitsubishi FA10S) was employed to machine the ECAP samples into square cross-sections with dimensions 10 mm × 10 mm × 80 mm. These samples were prepared from a solution-annealed ingot. After the WEDM process, the specimens were ground and polished using a Struers Labopol-25 to remove any cutting marks and ensure clean specimen surfaces for subsequent analysis. A mixture of graphite powder and molybdenum disulfide grease was applied to the specimens prior to the experiment to provide lubrication. The die utilized for the experiment is a three-piece split die housed in a square channel with a cross-section of 10 mm × 10 mm. The angle between the channels is 90° and the external curvature is 0°. The die is made up of high-strength tool steel, and the inlet and outlet channels have nearly the same dimensions. An INSTRON 100 kN UTM equipped with a heating chamber was used to apply pressure on the plunger, and a thermocouple was placed in the die to measure the temperature. Four passes were performed using Route Bc of ECAP, in which the billet is rotated by 90° in the same direction after each pass to promote a uniform and equiaxed ultrafine-grained microstructure, at a processing temperature of 290 °C.

2.3. Finite element modelling (FEM)

A three-dimensional (3D) finite element model of a single ECAP pass was developed using Abaqus/Explicit to simulate the deformation behaviour of a magnesium alloy at elevated temperatures. Because magnesium alloys exhibit a substantial loss of strength at elevated temperatures, even below 200 °C, the effect of temperature must be considered in the numerical analysis. However, fully coupled thermo-mechanical simulations are computationally demanding. Therefore, certain simplifications were introduced. In the experimental work, the ECAP process was conducted at 290 °C. Consequently, stress–strain curves obtained from compression tests (supporting information (Figure SF1)) at this temperature were implemented in the model.

An isothermal condition was assumed because the entire ECAP process was performed in a heated chamber, ensuring uniform initial temperatures of the billet, die, and punch. To mathematically justify this assumption prior to numerical modelling, the theoretical maximum adiabatic temperature rise (ΔT) was estimated. Based on the classical analytical model for an ECAP die geometry with a 90° channel angle, the theoretical equivalent plastic strain for a single pass is approximately 1.15. The necessary material flow behaviour at 290 °C was obtained by interpolating the experimental compression test data (provided in Supplementary Figure SF1). Using the interpolated flow stress (~120 MPa), the theoretical plastic work is approximately 138 MJ/m^3. Employing the Taylor-Quinney coefficient (β = 0.9), material density (ρ = 1710 kg/m^3), and an appropriate specific heat capacity for magnesium at elevated temperatures (Cp ≈ 1050 J/(kg·K)), the theoretical adiabatic rise is approximately 69.2 °C. However, this purely theoretical worst-case scenario assumes zero heat transfer. In reality, the low experimental punch speed of 0.1 mm/s implies a very low strain rate. At this velocity, the internal heat generated by plastic work has sufficient time to dissipate into the massive, pre-heated high-strength tool steel die, mitigating the potential for significant localized temperature increases. Finite element simulations of ECAP performed at comparable pressing speeds confirm that the actual temperature increase is extremely small. For example, Pei et al. [40] reported that when the pressing speed decreases from 18 mm/s to 0.18 mm/s, the peak temperature rise drops from approximately 44 K to only about 1 K due to enhanced heat dissipation. Therefore, under the even lower pressing speed used in the present study, the temperature rise can be considered negligible.

During the experiments, a mixture of graphite powder and molybdenum disulfide grease was applied to provide effective lubrication, a combination proven to significantly enhance frictional efficiency in metal forming operations [41]. Consequently, a low friction coefficient of μ = 0.04 was adopted in the simulations. This value accurately reflects realistic boundary conditions, as experimental ring compression tests confirm that effective solid lubrication reduces the friction coefficient to a range of 0.03–0.07 [42], a trend consistent with detailed friction analyses specific to the ECAP process [43].

To maintain good mesh quality despite the severe plastic deformation inherent to the ECAP process, the Arbitrary Lagrangian-Eulerian (ALE) adaptive meshing technique was applied to the entire billet volume. This is a standard and necessary approach supported by recent 3D FEM studies of magnesium alloys in the ECAP process, where ALE is successfully employed at identical low punch speeds (0.1 mm/s) to maintain mesh integrity and calculation accuracy under extremely high shear strains [44]. The assembly used in the model is shown in Fig. 2 below.

In the numerical model, the punch was defined as an analytical rigid surface, while the die was modelled as a discrete rigid shell body meshed with R3D4 (A 4-node 3-D bilinear rigid quadrilateral) elements. The billet was discretized using 7800C3D8R (8-node linear brick, reduced integration, hourglass control) solid elements. To reduce computational effort, symmetry along the Z-plane was utilized, modelling only half of the billet's thickness. The billet dimensions were 80 mm × 10 mm × 10 mm, while the die featured a square channel with a 10 mm × 10 mm cross-section. The channels intersect at an angle of 90°, and the outer curvature of the die corner was rounded to a radius of 2.5 mm to improve numerical stability and prevent mesh distortion.

Boundary conditions included fixing the die (Encastre) and allowing

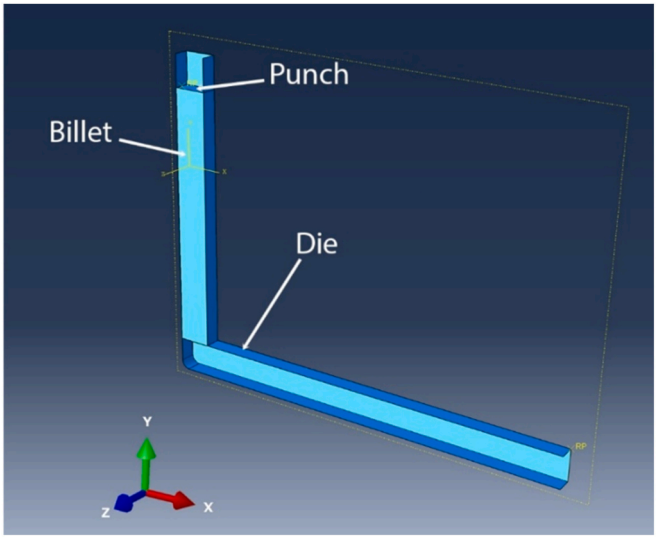

Fig. 2. Assembly of the ECAP set-up.

the punch to move only along the Y-direction. Surface-to-surface contact was specified between the billet and both the punch and the die, with finite sliding formulation. A penalty contact method was employed with the specified friction coefficient. The material properties applied in the numerical model are summarized in Table 2.

2.4. Characterizations

2.4.1. Mechanical

Flat tensile specimens for the tensile tests were machined from the initial annealed material and the ECAP-processed sample using wire electrical discharge machining (WEDM). The tests were performed with a crosshead speed of 8 μm/s, because the stage does not maintain a constant strain rate. The specimens had a 3 mm gauge length, gauge width of 2 mm and thickness of 2 mm, overall length of 50 mm, grip length of 10 mm, and grip width of 10 mm. Tensile tests were conducted by using a Kammrath & Weiss tensile and compression module (5 kN) on both the annealed and ECAPed samples. The tensile test specimens (three samples from each series) were placed in the tensile module. Additionally, a digital imaging correlation (DIC) setup with the KW stage and the Istra4D software interface was utilized. During these tests, the DIC Q-400 system by Dantec Dynamics was employed to observe the strain distribution during the tensile test.

2.4.2. Microstructural

The microstructural analysis including scanning electron microscopy (SEM) along with backscattered electrons for imaging and diffraction (EBSD) were carried out using a Keyence VHX-7000 digital microscope, and a high-resolution FEI Nova NanoSEM scanning electron microscope, which is equipped with a field emission gun and an EDAX system. The chemical composition of the corrosion products was analyzed by X-ray photoelectron spectroscopy (XPS) using a PHI VersaProbe II system with monochromatic Al Kα radiation (1486.6 eV) focused on a 100 μm spot. The take-off angle of photoelectron was set as 45°, and the analyzer pass energy was set to 117.50 eV for survey scans and 46.95 eV for high-resolution measurements. To maintain a consistent surface potential across samples with varying conductivity, a dual beam charge compensation technique was applied, involving 7 eV Ar^+ ions and 1 eV electrons. All XPS spectra were referenced to the C 1s peak of unfunctionalized saturated carbon (C–C) at 285.0 eV. The operating pressure within the analytical chamber was kept below 3×10^{-9} mbar. Deconvolution of the spectra was carried out using PHI MultiPak software (version 9.9.3), with the Shirley method employed for background subtraction. To further study the phases of the alloy, the X-ray diffraction study was conducted with a Bruker D8 Advance eco powder X-ray diffractometer using CuKα radiation (λ = 1.5418 Å), at a scanning rate of 2° per minute over a 2θ range of 10° to 70°.

2.5. Corrosion measurements

Electrochemical tests were carried out in 100 mL of Phosphate-Buffered Saline (PBS) solution (Sigma-Aldrich Chemie GmbH, Germany) containing 0.01 M phosphate buffered saline (0.138 M NaCl; 0.0027 M KCl) at pH 7.4 and 37 °C, utilizing a three-electrode cell configuration with a Gamry 600 Potentiostat/Galvanostat. The working electrode used was a magnesium alloy, while a platinum mesh was utilized as the counter electrode, and for the reference electrode an Ag/AgCl (3 M KCl) electrode was used. All samples were encased in a silicon rubber sheath, exposing a working surface area of 0.785 cm^2. The testing apparatus was housed within a Faraday cage to reduce electromagnetic interference. Electrochemical Impedance Spectroscopy (EIS) tests were carried out over a frequency range of 10^{-2} Hz to 10^5 Hz, with an amplitude of 10 mV at OCP after a prefixed immersion time (i.e., 1, 6, and 12 h). The data were analyzed using ZSimpWin software and fitted to an appropriate equivalent circuit. For Potentiodynamic polarization curves, tests were executed after the EIS measurement (e.g., immersion time 12 h) at a scan rate of 1 mV/s, from −200 mV vs. OCP to the anodic direction and stopped at an applied potential of +300 mV vs. OCP or after a sharp increase in the current. The i_{corr} (corrosion current density), E_{corr} (corrosion potential), β_c (cathodic Tafel slope), and β_a (anodic Tafel slope) were determined using Tafel extrapolation.

Table 2
Properties used in simulation for magnesium alloy [45,46].

Density [g/cm^3]	1.71
Poisson's ratio	0.35
Young's Modulus [GPa]	45

3. Results and discussion

3.1. Microstructural analysis

3.1.1. Heat-treated (HT) alloy

The presence of zinc (Zn) and calcium (Ca) as alloying elements, along with Si and Mn contaminants, can enhance corrosion resistance. Zn and Ca also facilitate the formation of high electrochemical potential phases, such as $Ca_2Mg_6Zn_3$. Literature indicates that maintaining a constant calcium presence of 0.2 wt% while varying zinc content between 0.4 wt% and 1.8 wt% enhances corrosion resistance. Micro-alloyed Mg-Zn-Ca systems exhibit α-Mg grains and strip-shaped phases of $Ca_2Mg_6Zn_3$ and Mg_2Ca at the grain boundaries, with a higher Zn/Ca ratio promoting the formation of these phases [47–50]. The SEM micrographs of the HT-alloy reveal a dendritic microstructure with Zn-bearing intermetallic phases localized at the grain boundaries, as depicted in Fig. 3(a) and Fig. S2. The occurrence of Zn segregation, consistent with previous observations [51], is evident in Fig. 3(a). Furthermore, backscattered electron (BSE) imaging highlights these intermetallics as brighter regions due to atomic number (Z) contrast (Fig. 3(b)). Point EDS analysis (Fig. 3(c)) reveals an elemental composition enriched in Ca, Mg, and Zn, suggesting the formation of a ternary Ca/Mg/Zn phase. Similarly, the EDS spectra presented in Fig. 3(d, e) indicates localized concentrations of Mg, Ca, and Si, which is consistent with the presence of MgCaSi phases. The intermetallic compounds are not formed by Mn and Mg; instead, Mn exists only in its elemental form [52,53]. Therefore, the intermetallic phases arise from the low solubility of silicon in the Mg matrix [26,54]. The presence of Mn has a negligible refinement effect on the alloy because it does not promote any nucleation during the solidification process [52]. In the initial material, which contains Si and trace amounts of Fe (measured at 0.0023 wt% via ICP-OES, Table 1), Si is highly prone to combining with Fe to precipitate highly cathodic FeSi intermetallic phases. Because the FeSi phase exhibits stronger cathodic activity than pure Fe or Mg2Si, it severely accelerates the micro-galvanic corrosion of the α-Mg matrix. However, the introduction of Ca fundamentally alters this precipitation sequence. Calcium exhibits a stronger thermodynamic affinity for Si than Fe does [55,56], acting as a preferential solute sink during solidification. Specifically, the formation enthalpy (ΔH) of the ternary MgCaSi phase is reported to be −137.95 kJ/mol (−0.48 eV/atom), which is significantly more negative than the −65.32 kJ/mol reported for the binary FeSi intermetallic [57,58]. Consequently, the addition of Ca effectively suppresses the precipitation of the hazardous FeSi phase by consuming the available Si to form the more thermodynamically stable MgCaSi compound. This microstructural transition preventing the formation of highly cathodic Fe-Si particles in favor of stable MgCaSi mitigates the severe micro-galvanic acceleration and significantly enhances the overall corrosion resistance of the HT-alloy [59]. The MgCaSi phase [60], resembles the $Ca_2Mg_6Zn_3$ phase; however, the MgCaSi phases are elongated or spherical in shape and are distributed within grains along the grain boundaries as shown in Fig. 3 and SF2.

The average grain size of the annealed alloy is ~235 μm in transverse and ~213 μm in the longitudinal direction as shown in Fig. 4. The large

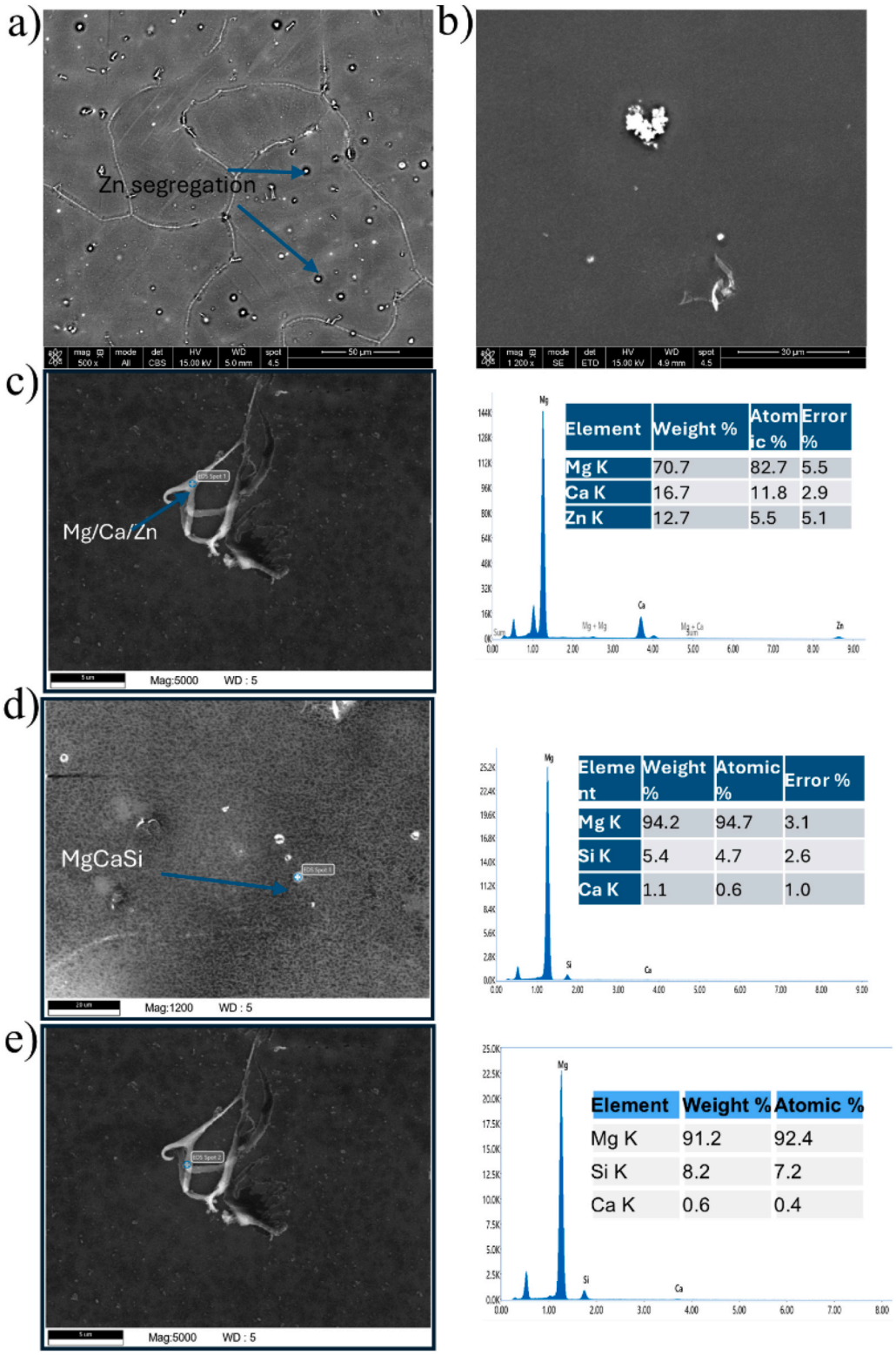

Fig. 3. SEM/EDS of HT-alloy **a)** Zn segregation is indicated, **b)** $Ca_2Mg_6Zn_3$ and Mg_2Ca brighter phases are visible, **c)** Point EDS analysis confirming the presence of the Ca/Mg/Zn phase, **d)** and **e)** Point EDS confirming Mg/Ca/Si phases.

grain size indicates that the strain distribution during the tensile test of the initial material is non-uniform due to its microstructure, caused by the relatively small cross-section of the samples. The observed twins in the microstructure may result from deformation during specimen preparation, as magnesium is highly sensitive to minor deformations. Analysis of the corresponding stereographic pole figures suggests that the initial annealed alloy exhibits a highly random texture. Additionally, the IPF (inverse pole figure) maps reveal a heterogeneous grain size distribution, with a notable presence of both fine and coarse grains. This variation in grain size is critical, as finer grains typically contribute to improved strength through grain boundary strengthening mechanisms, while larger grains may enhance ductility.

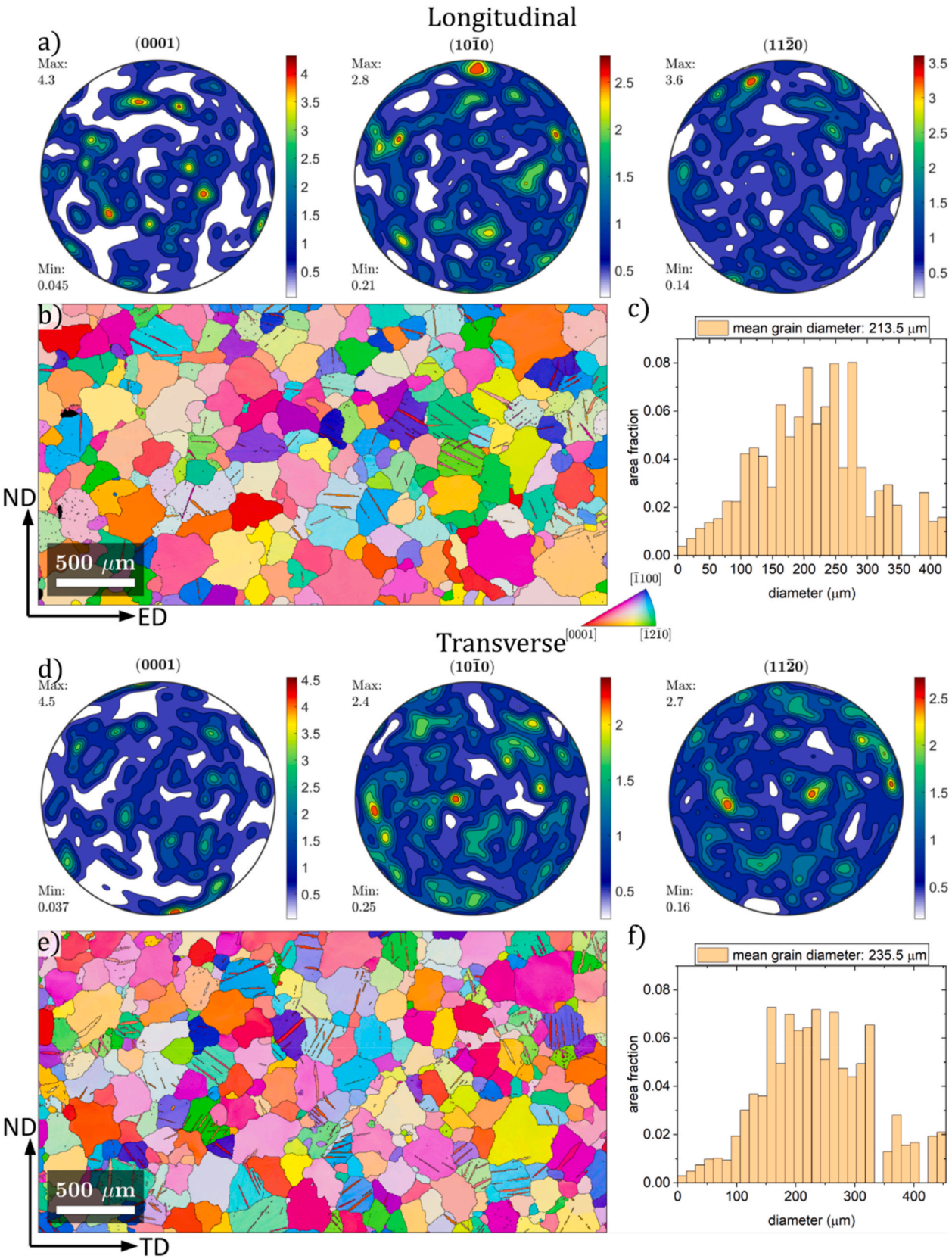

Fig. 4. Microstructure of the Mg–Ca–Zn system before ECAP. Longitudinal direction: **(a)** pole figures, **(b)** IPF TD orientation map, **(c)** grain size distribution. In transverse direction: **(d)** pole figures, **(e)** IPF ED orientation map, **(f)** grain size distribution.

3.1.2. ECAP microstructure

The microstructure of the specimens processed through Equal Channel Angular Pressing (ECAP) is depicted in Fig. 5(b–e). Following ECAP, the alloy exhibits equiaxed grains with an average size of approximately 6.5 μm in the longitudinal direction as shown in Fig. 5(c). In the transverse section, the microstructure predominantly comprises fine grains, with size approximately 4.83 μm as shown in Fig. 5(f). The average sub-grain size of the ECAP-alloy is around 4 μm in the longitudinal direction and 3.4 μm in the transverse direction as shown in Figure SF3 (supporting information). EBSD based pole figures present a rather typical texture for a magnesium alloy processed by route Bc in ECAP [61]. This is consistent with typical texture evolution, where after first ECAP pass the 0001 pole is aligned in the ND ED plane, and tilted about 55° away from the ED direction. In subsequent ECAP passes the maximum in 0001 pole figure is tilted away from the ND ED plane towards the TD axis, due to 90° rotation of the billet in Bc ECAP route. This supports the conclusion that deformation during ECAP processing is dominated by dislocation glide in the basal slip system.

After the ECAP processing at a die angle of 90°, a significant reduction in grain size was observed. The microstructure was effectively refined through dynamic recrystallization, which was accompanied by severe shear deformation resulting from the ECAP process. Analysis of the stereographic pole Fig. 5(a, d) indicates that the alloy developed a pronounced texture after ECAP. In the longitudinal section, regions with small equiaxed grains coexist with larger grains that are elongated in the direction of pressing, representing remnants of the original deformed elongated grains. Fig. 5(g, h) illustrates the distribution of grain boundary misorientation. Misorientation angles greater than 15° are associated with high-angle grain boundaries, indicating a transition of the material from low-angle to high-angle grain boundaries due to the substantial deformation experienced during ECAP. This recrystallization stage, facilitated by dislocation accumulation and fine-grained integration, promotes a homogeneous microstructure characterized by an ultrafine-grained appearance after four passes of ECAP. The elevated proportion of high-angle grain boundaries contributes to the formation of a uniform and protective coating on the magnesium surface, effectively reducing its corrosion rate as discussed in a later section.

Additional analysis of Schmid factors (SF) was conducted to provide possible rationalization for yield point differences between ECAPed and HT samples. SF histograms and maps are presented in Fig. 6. Histograms present the complete distribution, while maps were filtered to show only grains with SF $>$ 0.2. The SF values distribution is similar in both samples, with a strong peak above SF $>$ 0.4 indicating a large fraction of grains oriented favorably for basal slip. Due to relatively high critical resolved shear stress (CRSS) of non-basal slip systems in Mg alloys, the basal dislocation system is activated even in grains with relatively low SF values. However the differences in fraction of grains with SF $>$ 0.2 between HT sample (76.5%) and ECAP sample (68.5%), can help to partially explain much higher yield point in ECAP sample, as grains with the lowest basal SF have to activate additional slip systems, such as 2nd order pyramidal <c+a> [62], while tensile twinning is most likely suppressed in ECAP sample due to grain refinement [63]. Activation of pyramidal slip system can then promote cross-slip leading to increased dislocation interactions and strain hardening rate in ECAP sample [64]. On the other hand, the HT sample has slightly higher fraction of high basal SF grains and its plasticity is enhanced strongly due to possibility of tensile twin activation in large grains [65].

3.2. FEM

The evolution of the equivalent von Mises stress during the ECAP process is presented in Fig. 7, which shows three snapshots capturing successive stages of billet deformation. At the initial stage (Fig. 7(a)), as the billet enters the intersection of the die channels, elevated stress concentrations are observed at the billet's outer corner regions in contact with the die walls. This is due to the intense shear deformation imposed as the billet begins to change its flow direction through the 90° channel angle. As the process progresses (Fig. 7(b)), the zone of high equivalent stress propagates deeper into the billet, following the shear plane imposed by the die geometry. In the intermediate stage, stress intensities remain significant along the billet's diagonal plane, reflecting the dominant simple shear mechanism typical for ECAP. In the final stage (Fig. 7(c)), as the billet exits the die corner and progresses into the outlet channel, the stress distribution becomes more uniform. However, localized stress concentrations persist near the billet's outer surfaces, showing that the severe plastic deformation during passage through the die corner continues to influence the billet's stress distribution.

Fig. 8 illustrates the distribution of the equivalent plastic strain (PEEQ) at the same three stages of the ECAP process. Initially (Fig. 8(a)), plastic strains are concentrated near the die corner where the billet first contacts the channel intersection, reflecting the onset of shear deformation. As the billet advances further through the corner (Fig. 8(b)), the region of elevated PEEQ expands, clearly delineating the shear plane formed at the 90° intersection of the channels. In the final stage (Fig. 8 (c)), the strain field stabilizes, showing a band of high plastic strain extending diagonally across the billet cross-section. This characteristic strain pattern confirms that the billet has undergone significant simple shear deformation, which is the fundamental mechanism responsible for grain refinement in the ECAP process. Overall, the simulation results for PEEQ are consistent with the expected material flow and deformation characteristics during ECAP.

The simulated punch force as a function of time is shown in Fig. 9. The punch force increases steadily as the billet enters the die corner, reaching a peak value of approximately 40 kN. Subsequently, the force slightly decreases and stabilizes as the billet passes through the corner and progresses into the outlet channel. The maximum predicted force from the simulation is in close agreement with the experimental measurement of approximately 39 kN (supporting information SF4), demonstrating the validity and accuracy of the developed finite element model. This good correlation confirms that the chosen material model, friction conditions, and boundary constraints accurately capture the mechanical response of the ECAP process.

The stress and strain distributions obtained from the simulations are consistent with patterns reported in previous studies of ECAP-processed materials. In particular, the formation of a distinct shear band along the 45° plane through the billet cross-section, visible in the PEEQ contours (Fig. 8), corresponds well with observations in the literature, where similar shear zones have been identified as the primary regions of intense plastic deformation and grain refinement during ECAP [66,67]. Studies by Segal [67] and Iwahashi et al. [66] have highlighted that this shear plane is the dominant mechanism for imparting large strains into the material, promoting microstructural evolution and texture development. The simulated von Mises stress distribution (Fig. 7) also shows elevated stress concentrations along this shear plane, further confirming the agreement between the numerical results and experimental findings. While the macroscopic kinematics align with existing literature, the added value of the present FEM analysis lies in the material-specific quantitative prediction of the deformation behaviour. By directly incorporating experimental stress-strain data from isothermal compression tests of the investigated Mg-Zn-Ca alloy, combined with the ALE adaptive meshing technique to prevent volumetric locking and element distortion, the model accurately captures the required punch force. Overall, the present simulation results corroborate the characteristic deformation behaviour of ECAP, demonstrating the formation of high shear strain bands and localized stress fields associated with the billet's passage through the die corner. Furthermore, the model validates the specific mechanical response of this investigated material.

3.3. Mechanical test

Several studies reported that grain refinement improves the mechanical properties of magnesium alloy [68]. It improves ductility by

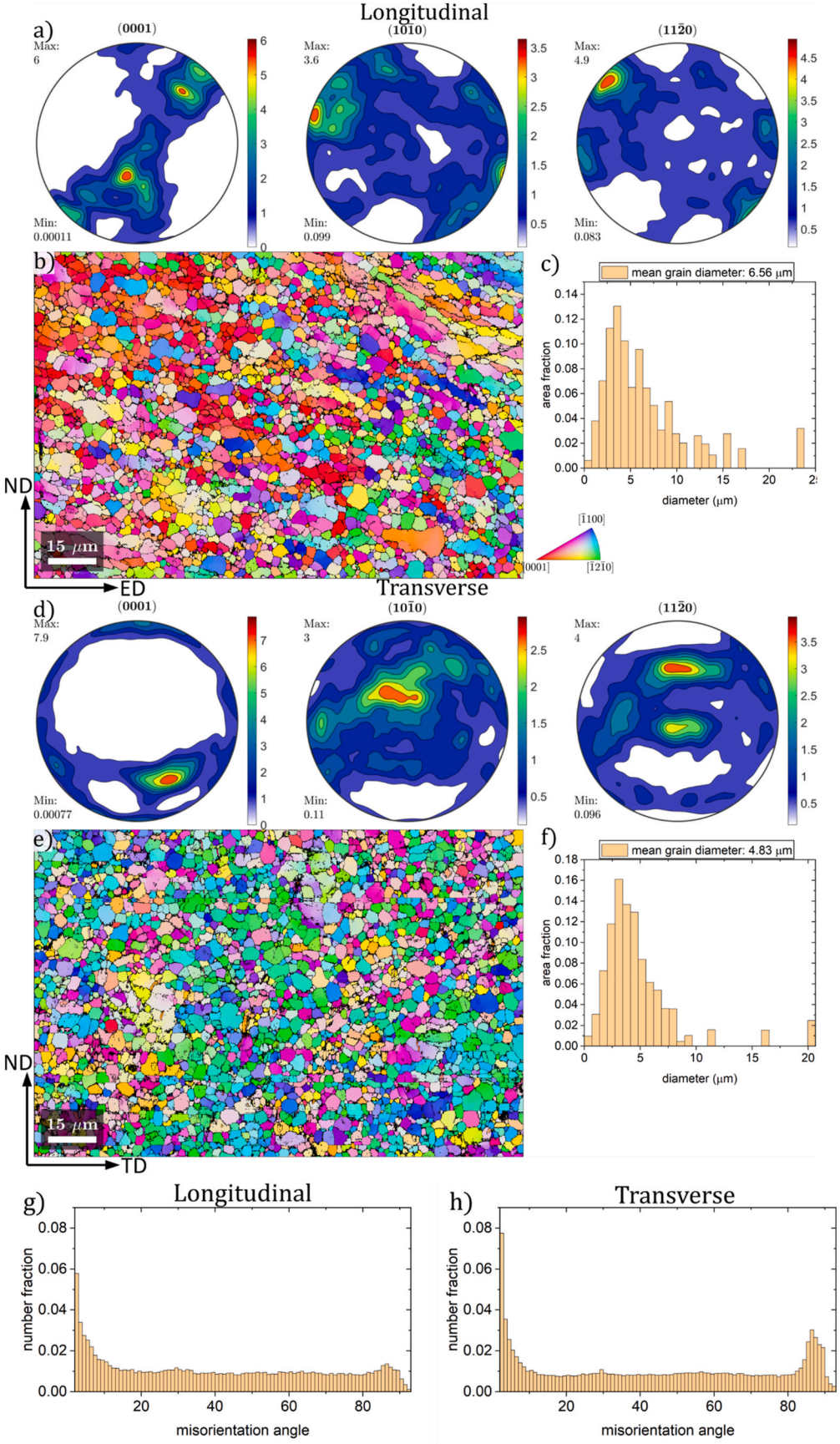

Fig. 5. Microstructure of the Mg–Ca–Zn system after ECAP in the longitudinal direction: **(a)** pole figures, **(b)** IPF TD orientation map, **(c)** grain size. In the transverse direction: **(d)** pole figures, **(e)** IPF ED orientation map, **(f)** grain size. **(g)** and **(h)** show misorientation angles.

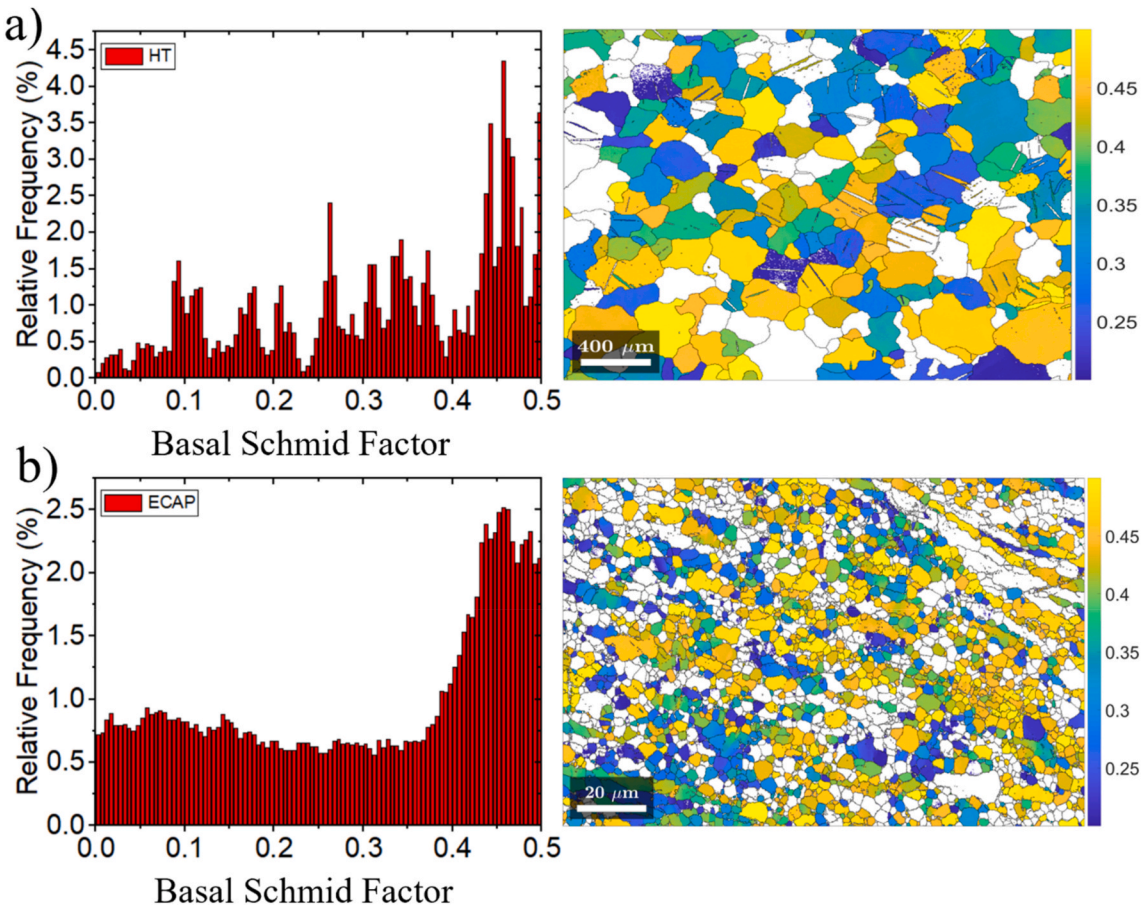

Fig. 6. Schmid factor for basal slip system in **a)** HT and **b)** ECAP processed Mg alloy. Corresponding Schmid factor maps present only grains with SF > 0.2.

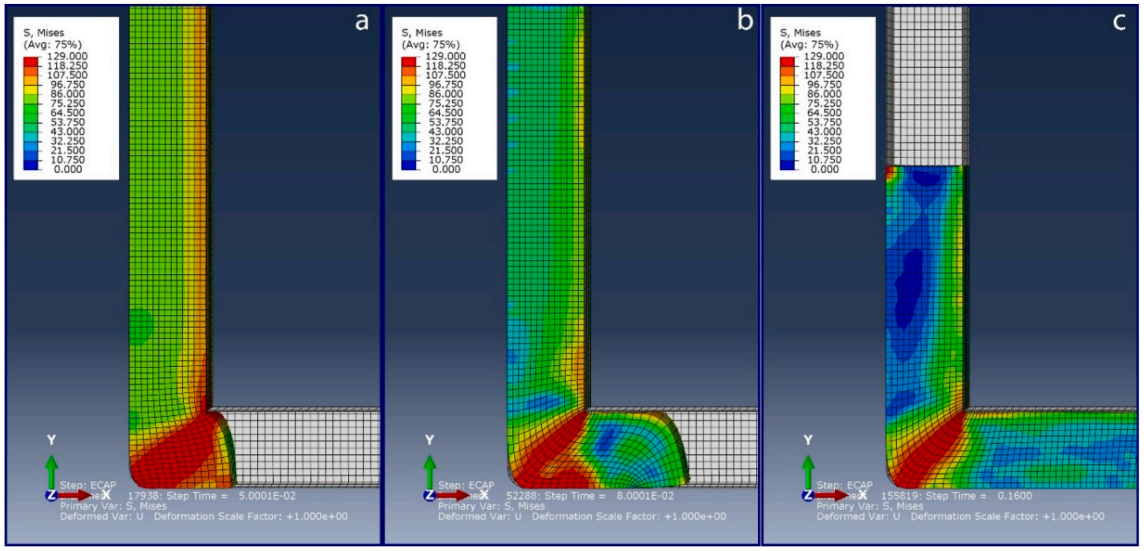

Fig. 7. Equivalent von Mises stress distribution in the billet during successive stages of the ECAP process.

inhibiting the twinning mechanism, which can lead to strain localization and strain hardening [69,70]. This localization may result in the nucleation and growth of voids, ultimately causing mechanical failure [71–74]. When the grain size is sufficiently refined, the critical resolved shear stress (CRSS) for twinning can exceed that of prismatic or pyramidal slip systems. This dynamic helped to reduce twinning activity, thereby contributing to improved ductility [75]. The results of tensile tests at room temperature are shown in Fig. 10. The ultimate tensile strength of the initial material is 226 MPa, as represented in the stress vs. strain plot. It can be observed that the alloy exhibits an increase in ultimate tensile strength to 290 MPa after the four-pass ECAP process, compared to the initial material. After ECAP, the material shows ultimate tensile and yield strengths of 290 MPa and 234 MPa, respectively. There is not much change in the elongation of the material before and

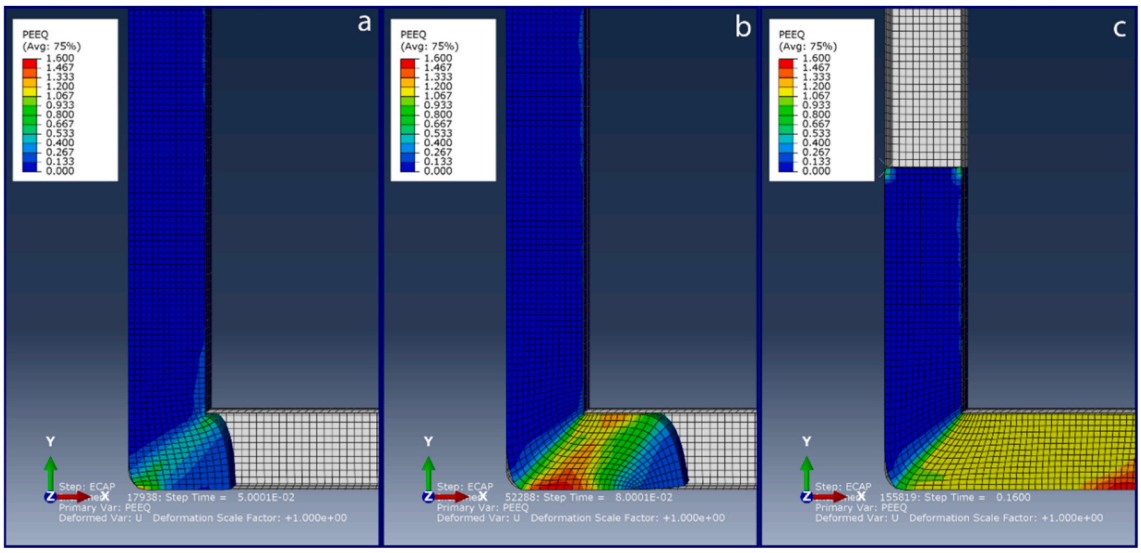

Fig. 8. Distribution of equivalent plastic strain (PEEQ) in the billet at different stages of the ECAP process.

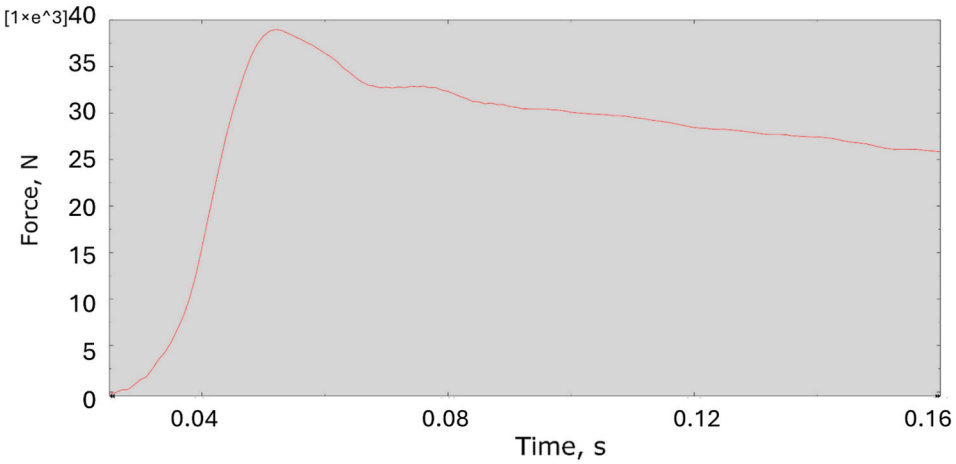

Fig. 9. Simulated punch force versus time curve for the ECAP process.

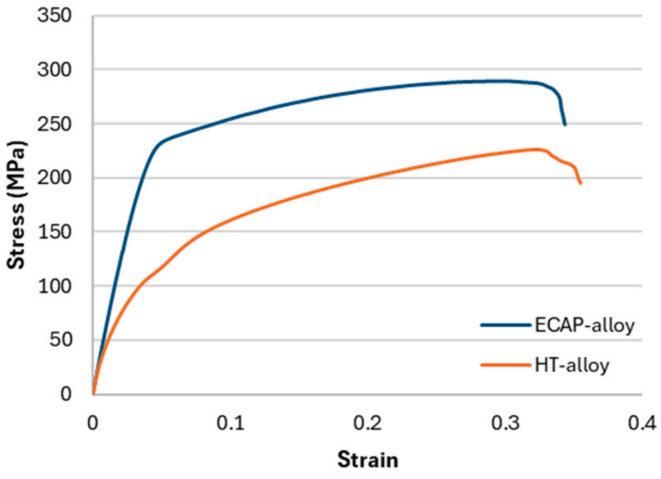

Fig. 10. Stress-strain curve at room temperature for HT and ECAP alloy.

after ECAP, which is approximately 37% and 35%, respectively. This shows that the elongation at break is not purely dependent on the grain size of the material, as the texture appears to have a negative influence on ductility in the ECAP state. In contrast, the tensile strength is directly dependent on the grain size, as the microhardness of the alloy and its strength increased after four ECAP passes due to grain refinement, and strain hardening [76].

The yield point phenomenon [77], which does not occur in the initial material's stress-strain curve, is a notable characteristic of the engineering tensile stress-strain curves of ECAP alloy as shown in Fig. 10. Further movement requires less stress after the dislocations have been released by a high enough tension. The absence of movable dislocations in Mg alloys with small grain sizes provides another explanation. Dislocation sources must be activated in order to start plastic deformation, which takes more stress than just deformation. Some studies also suggested that the occurrence of yield point phenomena is caused by deformation twinning. In the early stages of plastic deformation, twinning is a significant deformation mechanism in magnesium alloys. It causes an abrupt drop in stress within a grain, which can then cause twinning in nearby grains, and promotes slip deformation in initially unfavorably orientated grains. Possibly other causes, or it could be multiple mechanisms, may be at work to cause the yield point phenomenon in various magnesium alloys [78].

Utilizing the DIC approach, the true effective and true principal strain distributions during the tensile test were examined. The outcomes are shown in Fig. 11 for the received HT alloy and after ECAP,

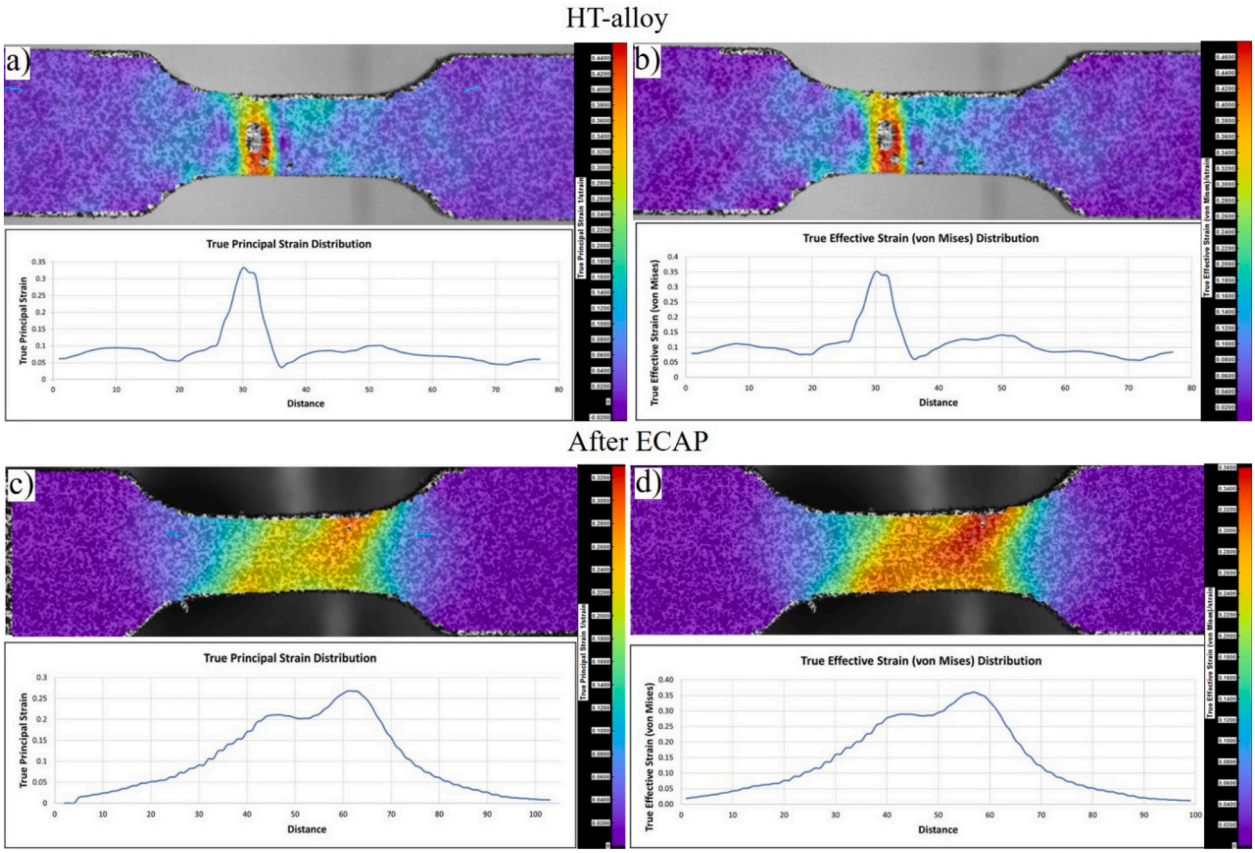

Fig. 11. True principal strain distributions for HT and ECAP alloys are shown in (a) and (c), respectively, while effective strain distributions for HT and ECAP are shown in (b) and (d), respectively.

respectively. The initial material's (Fig. 11(a and b)) strain distribution is not uniform and is positioned on one side of the gauge length rather than concentrated in the middle. This indicates that the alloy's structure is not homogenous and has higher grain sizes. Because of the higher grain size, it is easier to initiate the dislocations, but it becomes difficult to propagate them to neighboring grains resulting in strain concentration at specific point or area. While the fracture was predominantly in the middle of the ECAP-processed material, it happened away from the center in the initial material because of the smaller grain sizes. In contrast to the initial material, the ECAP sample's true effective and true principal strain distribution is depicted in Fig. 11 (c, d) as being more uniform and dispersed across the gauge length. Such behavior is a result of the alloy's altered structure and refined grain structure undergoing ECAP deformation. This change in microstructure helps in strain-hardening and the crystal structure of the sample has accumulated dislocation that acts as a stopping point for further dislocations to take place thus increasing the strength of the alloy. These findings demonstrate that stress increase as grain size is reduced. The yield strength, ultimate tensile strength, and strain distribution during the test are all mechanical properties that are significantly impacted by grain size variation.

3.4. *Electrochemical corrosion tests*

Time sequential EIS tests were conducted to understand the corrosion behaviour of ECAP and HT alloys in PBS solution, at intervals of 1,

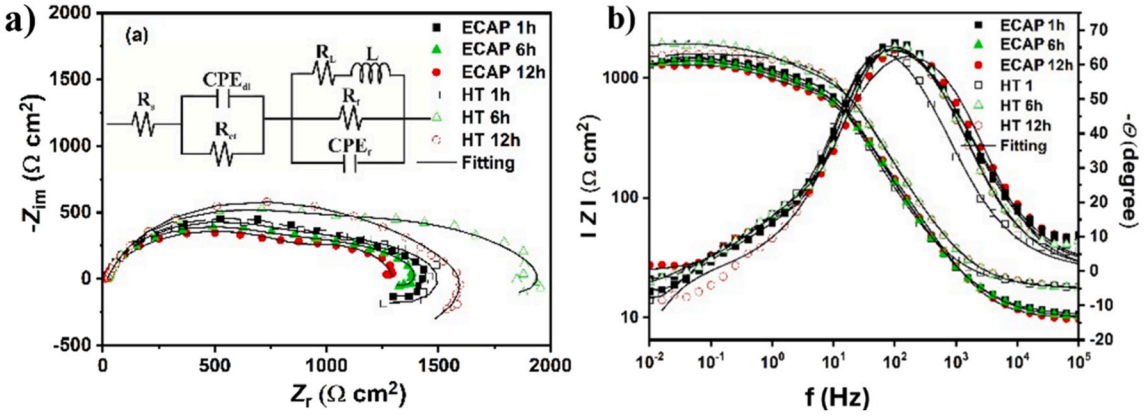

Fig. 12. **(a)** Nyquist and **(b)** Bode plots of the HT alloy and ECAP alloy.

6, and 12 h. Fig. 12 (a, b) illustrates the Nyquist and Bode plots for these samples. The EIS plots show that both ECAP and HT alloys exhibit similar electrochemical behavior, featuring a large capacitive loop at high frequencies (HF), a small capacitive loop at medium frequencies (MF), followed by an inductive loop at low frequencies (LF) [23,79,80]. The HF capacitance loops are typically associated with the charge transfer process at the metal/solution interface, while the MF loops relate to the development of the surface corrosion film, respectively. Lastly, the LF inductive loop is generally associated with relaxation processes caused by species adsorption at the corrosion layer and/or the onset of pitting corrosion. The experimental data were fitted using the electrical equivalent circuits (EEC) shown in the inset Fig. 12(a), and Table 3 contains the fitting results. The EEC used consisted of solution resistance (R_s); the constant phase element of the double-charge layer capacitance, and the charge transfer resistance (CPE_{dl} and R_{ct}); the constant phase element and resistance of the corrosion products film (CPE_f and R_f), and the inductive loop and its resistance (L and R_L) [23,79,81]. A constant phase element (CPE) is utilized in the EEC to account for the non-homogeneous nature of electrode surfaces in corrosion studies, particularly for magnesium alloys in phosphate-buffered saline (PBS) solutions. It consists of two parameters: Q, which reflects capacitance-like behavior influenced by surface defects, and n, the dispersion index ranging from 0 to 1, where higher values indicate smoother surfaces and lower values suggest rougher, more porous surfaces [23,79,81–83]. Low χ^2 values indicate that the EEC effectively captures the corrosion phenomena and validates its accuracy.

The following reactions can illustrate the overall deterioration of Mg alloys in the PBS solution:

$$\text{Anodic reaction}: Mg \rightarrow Mg^{2+} + 2e^- \quad (1)$$

$$\text{Cathodic reaction}: 2H_2O + 2e^- \rightarrow H_2 + OH^- \quad (2)$$

$$Mg^{2+} + OH^- \rightarrow Mg(OH)_2 \quad (3)$$

The overall degradation reaction of Mg:

$$Mg + 2H_2O \rightarrow Mg(OH)_2 + H_2 \quad (4)$$

Based on the literature [23,79,83,84], two distinct layers develop on the Mg alloy surface: an initial thin MgO barrier layer formed immediately when the metal contacts PBS solution, then a thicker porous Mg $(OH)_2$ layer that covers the MgO. The magnesium and hydroxide ions then lead to the formation of $Mg(OH)_2$ (Eq. (3)).

Data indicates that during the initial hours of the experiment, the HT sample exhibits higher R_{ct} and R_f values compared to the ECAP-processed sample. This suggests that the charge transfer in the corrosion processes (e.g., Eqs. (1) and (2)) for the HT processed sample was slowed down due to the formation of the $Mg(OH)_2$ layer. With increased immersion time, the R_{ct} decreased. The chloride ions penetrate the matrix, converting the $Mg(OH)_2$ layer into soluble $MgCl_2$, which then dissociates into Mg^{2+} and Cl^-, resulting in deeper corrosion of the matrix.

$$Mg(OH)_2 + 2Cl^- \rightarrow MgCl_2 + 2OH^- \quad (5)$$

Therefore, the reduction in the R_{ct} value could result from Mg dissolving through pores or imperfections in a less-dense passive layer. Conversely, R_{ct} and R_f values for the ECAP-processed sample were relatively stable with immersion time.

It is worth noting that there is no consensus on how grain refinement influences the corrosion resistance of Mg alloys. Some studies indicate that grain refinement may decrease corrosion resistance [85,86], whereas others suggest it enhances it [87]. Palumbo et al. [88] found that as grain refinement increases, so does the volume fraction of intercrystallite regions like grain boundaries and triple junctions. These boundaries and junctions possess higher energies than the bulk material, making them more chemically active with the surrounding matrix. Consequently, refining the grains boosts the surface reactivity, potentially leading to the preferential dissolution of grains. The varying consensus in the literature arises from the difficulty of isolating the effect of grain refinement from other microstructural changes induced by the process (e.g., the alloy's crystallographic orientation, the presence and distribution of secondary phases). In this study, while both alloys undergo electrochemical dissolution in chloride-rich media, their dominant mechanisms are influenced differently by their respective microstructures. The HT-alloy primary mechanism features a lower density of grain boundaries, resulting in slower initial surface reactivity. The coarser structure does not support the rapid formation of a cohesive protective layer, leading to more sustained charge transfer between the electrolyte and the metal matrix. The dominant mechanism of the ECAP alloy is driven by the high-volume fraction of intercrystallite regions (grain boundaries and triple junctions). Although these regions have higher energy and are more chemically active, this increased reactivity promotes rapid nucleation and growth of a compact corrosion product layer. This layer serves as an effective physical barrier, stabilizing the corrosion process from the beginning [81].

The polarization curves are shown in Fig. 13, and the Tafel parameters are listed in Table 4. The Corrosion performance of both samples largely depends on the I_{corr} values. Lower I_{corr} values signify better corrosion performance. The potentiodynamic measurements are in agreement with the EIS observations. The data shows a slight change in i_{corr} between both samples after 12 h of immersion in PBS solution, suggesting that the grain refinement process did not significantly alter the corrosion resistance of the HT alloy. Both samples exhibit a small passivity range in the tested PBS solution due to the formation of the Mg $(OH)_2$ film. As mentioned earlier, the $Mg(OH)_2$ film is unstable in the presence of Cl^- ions, leading to localized pitting corrosion. The Fig. 13 shows that the ECAP-treated sample is less prone to pitting corrosion, with a pitting potential (E_{pit}), (−1.48 V), being more positive than that of the HT sample (−1.39 V). ECAP treatment reduces grain size, improving microstructure uniformity and resulting in a stronger oxide film, thereby decreasing localized corrosion.

Table 3
EIS parameters for the HT alloy and ECAP alloy in PBS solution.

Time (h)	R_s (Ω cm^2)	CPE_{dl}		R_{ct} (Ω cm^2)	CPE_f		R_f (Ω cm^2)	L (H cm^{-2}) x10^{-4}	R_L (Ω cm^2)	$R_p = R_{ct} + Rf$ (Ω cm^2)	χ2 (10^{-3})
		Q_{dl} (μΩ^{-1} cm^{-2} s^n)	n_{dl}		Q_f (μΩ^{-1} cm^{-2} s^n)	n_f					
HT											
1	17.80	325.40	0.63	1035	24.16	1.000	566	0.81	101	1601	0.72
6	17.41	169.80	0.66	1347	11.17	0.990	648	2.68	671	1995	0.51
12	19.92	109.70	0.70	941	17.53	0.996	657	2.18	100	1598	1.59
ECAP											
1	10.39	31.64	0.62	882	22.70	0.976	665	1.31	575	1547	0.69
6	9.85	29.90	0.62	961	23.76	0.981	515	1.15	620	1476	0.54
12	9.13	396.70	0.61	934	23.30	0.962	501	0.69	959	1435	0.18

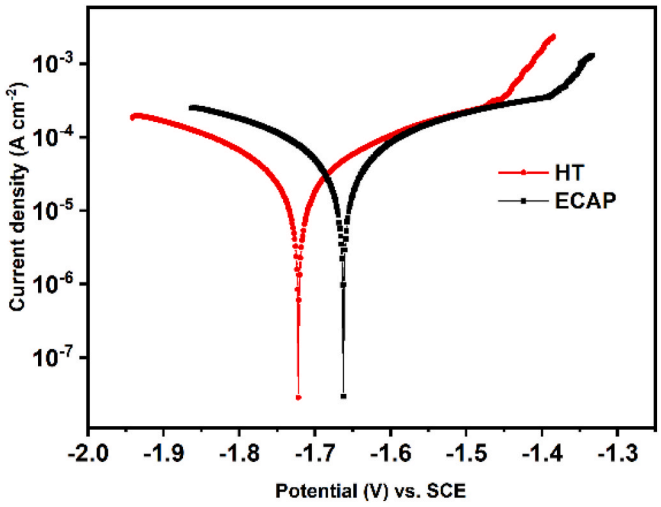

Fig. 13. Potentiodynamic polarization curves of the HT and ECAP alloys in PBS solution.

Table 4
Potentiodynamic polarization data of the HT and ECAP alloys in PBS solution.

Sample	β_c (V dec^{-1})	β_a (V dec^{-1})	i_{corr} (μA cm^{-2})	E_{corr} (V)	E_{pit} (V)
ECAP	0.337	0.352	75.40	−1.66	−1.48
HT	0.275	0.275	77.40	−1.72	−1.39

3.5. Micro scale analysis

After immersion for 24 h in PBS solution, the samples exhibited significant corrosion, as illustrated in Fig. 14. The corrosion product layers covered the entire surface and displayed several deep cracks. The SEM images reveal corrosion pits on both the ECAP and HT alloys. At higher magnification (Fig. 14(c)), the HT alloy exhibits deeper pits that are observed more frequently compared to the smaller and less frequent pits found in the ECAP alloy (Fig. 14(f)), demonstrating the better pitting corrosion resistance of the ECAP alloy surface. The surface corrosion morphology in both samples is uneven; however, the HT alloy surface is flatter than that of the ECAP alloy at lower magnification (Fig. 14), indicating a more effective distribution of the protective film in the HT alloy. This improved distribution is likely due to the heat treatment process, which enhances the alloy's microstructure and promotes better film formation. Furthermore, the overall oxygen percentage in the EDS spectra is higher for the ECAP processed alloy, as shown in the supporting information (Figure SF5 & SF6).

The chemical composition, as shown in the EDS spectra, primarily consists of Mg, Ca, Zn, O, and P, along with MgO and $Mg(OH)_2$ films. The presence of metal phosphate and carbonate compounds is also speculated, which is later confirmed by XPS analysis. Specifically, the formation of $Mg_3(PO_4)_2$ leads to the development of a gel-like barrier that subsequently crystalizes, thereby contributing to the protective layer, while $MgHPO_4.3H_2O$ forms a crystalline and stable hard shell that slows down corrosion in both cases [89]. Without the presence of calcium ions, which are essential for the formation of a complex apatite layer, the corrosion resistance of the material becomes dependent solely on the stability of the magnesium-phosphate barriers. These barriers play a crucial role in protecting the substrate from aggressive chloride ions.

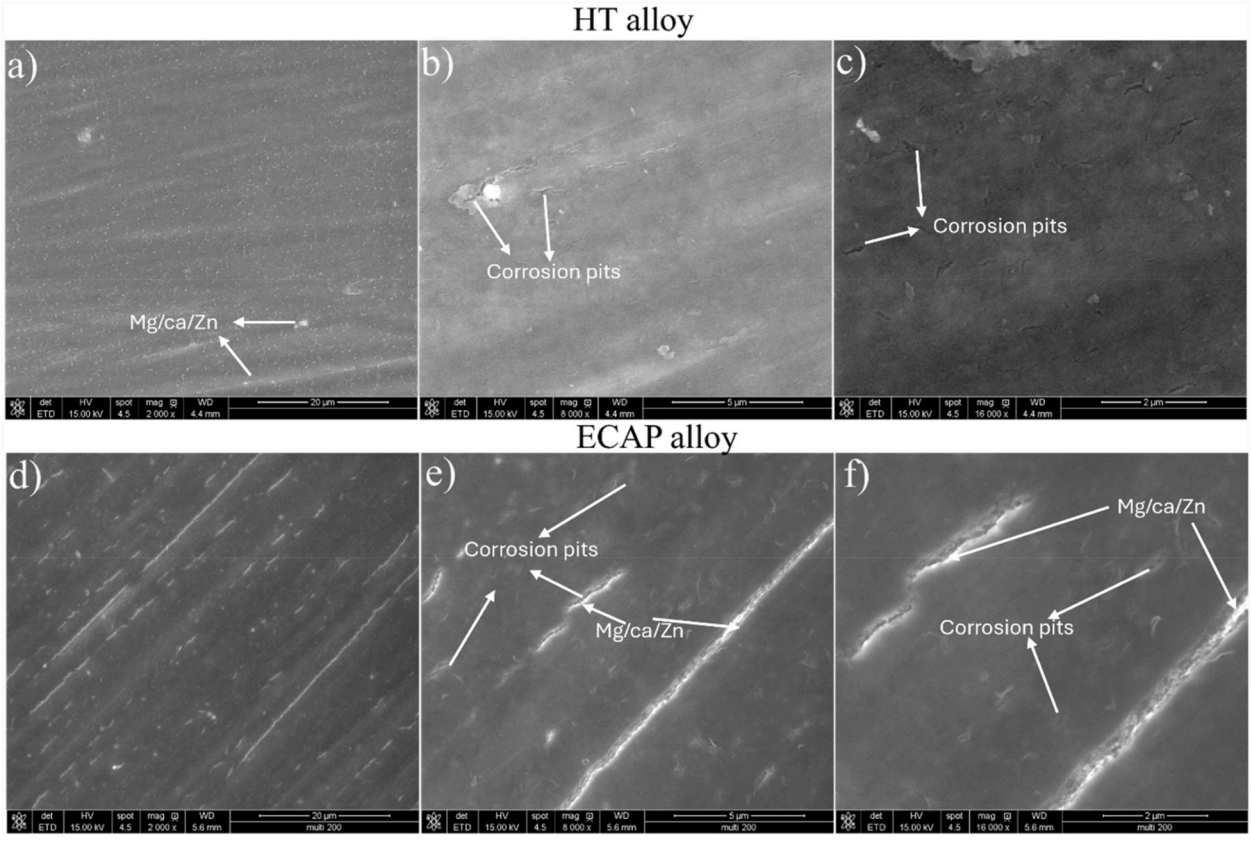

Fig. 14. **(a–c)** SEM morphology of heat-treated sample and **(d–f)** ECAP processed samples after 24-h immersion in PBS solution at different magnification.

Furthermore, SEM images in figure show that the brighter regions containing the $Ca_2Mg_6Zn_3$ phase are still present in both ECAP and HT alloy samples, while the Mg_2Ca phase has completely dissolved. The point EDS spectra in the supplementary information figure SF7 for the brighter phases ($Ca_2Mg_6Zn_3$) in both alloys reveal a very low oxygen percentage, further confirming the corrosion-resistant nature of $Ca_2Mg_6Zn_3$ phase. The differences in corrosion susceptibility among these phases can be attributed to their positions in the galvanic series. The Mg_2Ca phase, having a more negative Volta potential, acted as the anode and corroded preferentially. In contrast, the $Ca_2Mg_6Zn_3$ and MgCaSi phases, with more positive potentials, functioned as cathodes, thereby facilitating the galvanic corrosion process [51,90,91]. According to Xu et al. [92], even little presence of Mn in magnesium alloys affects the microstructure and improves the corrosion resistance. It increases the magnesium-containing phosphates, which form a protective layer and provide protection against the corrosive attack of ions [93]. Additionally, the XRD patterns for both HT and ECAP alloys investigated are illustrated in supporting information (Figure SF8). Each alloy exhibits prominent peaks associated with the α-Mg phase, alongside weaker peaks attributed to the secondary phases Mg_2Ca and $Ca_2Mg_6Zn_3$.

Both sample surfaces covered with corrosion deposits due to 24 h immersion in PBS were subsequently analyzed in terms of detailed chemical states using the XPS technique [94]. Fig. 15(a) illustrates survey scans acquired to reveal the general elemental composition of the obtained deposits.

The collected XPS survey scans revealed the same elemental lines in both tested samples, i.e. C, K, Mg, Ca, P, Cl, Na and O, with different signal intensities. Namely, in the HT alloy, the intensity of signals originating from the elements contained in the PBS structure is higher, which is well correlated with previous SEM results and confirms a more preferential microstructure of the sample for forming the passivation-like layer. Further, the chemical species of elements in these deposits were identified by curve-fitting of high-resolution spectra acquired in the regions of the main elemental lines, as shown in Fig. 15(b–h).

The C 1s spectra for analyzed samples were fitted with four components. First line was found at 285.0 eV which indicates C-C and C-H bonds, second line at 286.4 eV represents C-O-C and/or C-OH groups, third line positioned at 287.9 eV corresponds to C=O groups, while the

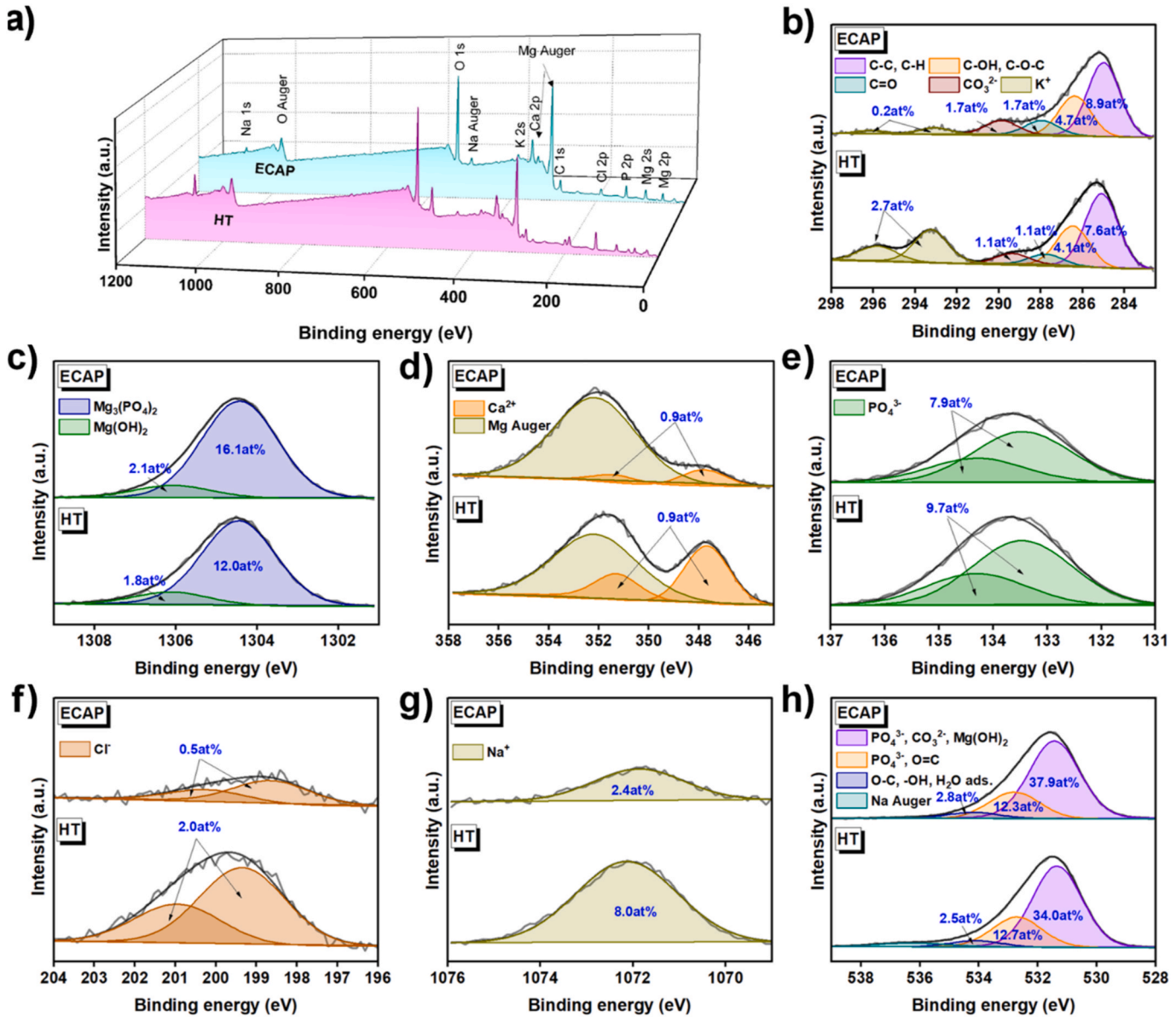

Fig. 15. **a)** Wide-range survey scans, and high-resolution XPS spectra acquired in **b)** C 1s + K 2p, **c)** Mg 1s, **d)** Ca 2p, **e)** P 2p, **f)** Cl 2p, **g)** Na 1s and **h)** O 1s regions, for the ECAP and HT alloys immersed in PBS solution for 24h.

last line observed at 289.5 eV indicates CO_3^{2-} species [95,96]. The K 2p spectra were fitted with one doublet structure ($2p_{3/2}$–$2p_{1/2}$ separation 2.7 eV) with the main $2p_{3/2}$ line at 293.3 eV which indicates K^+ ions like in K_3PO_4 and/or KCl [97]. The Mg 1s region was fitted with two lines, with the first line at 1304.5 eV indicating Mg^{2+} cations like in $Mg_3(PO_4)_2$, $MgHPO_4.3H_2O$ and $Mg(OH)_2$ compounds with possible fractions of MgO and/or $MgCl_2$, and second at 1305.9 eV corresponding to magnesium hydroxide [97,98].

The spectra collected in the Ca 2p region were fitted with a doublet structure with $2p_{3/2}$–$2p_{1/2}$ splitting 3.51 eV with the main 2p3/2 line at 347.8 eV which represents Ca^{2+} ions like in either $Ca_3(PO_4)_2$ or $CaCO_3$ and small amounts of CaO species [97]. The spectra in P 2p region, were fitted with doublet structure ($2p_{3/2}$–$2p_{1/2}$ splitting equals 0.84 eV) with the main $2p_{3/2}$ line at 133.4 eV indicates P^{5+} oxidation state like in PO_4^{3-} [95]. The Cl 2p regions were fitted with doublet structure (doublet separation $2p_{3/2}$–$2p_{1/2}$ equals 1.6 eV) with the main $2p_{3/2}$ line at 198.9 eV which indicates presence of Cl^- ions in chlorides like in e.g. $MgCl_2$ and KCl, [95,97]. The Na 1s spectra were fitted with a single line centered at 1072.0 eV represents Na^+ ions like in Na_2CO_3 and $Na_3(PO_4)_2$ compounds [97]. The O 1s spectra for samples were fitted with three components. The first line observed at 531.5 eV indicates O-Mg type bonds in magnesium oxide and/or hydroxide and O-C bonds in carbonates and/or PO_4^{3-}, second line at 532.7 eV points out the existence of PO_4^{3-} and/or O=C bonds in organic compounds and the last line at 533.9 eV can originate either from O-C and/or O-H bonds and/or adsorbed H_2O [95,97].

Considering the results of XPS and SEM-EDS measurements, the deposited films are found to contain precipitated phosphate and carbonate salts, formed through interactions among the oxide and hydroxide products of magnesium, calcium, and zinc. These protective films enhanced the pitting resistance due to the interaction among the oxide and hydroxide products of magnesium, calcium, and zinc [99]. However, the higher concentration of inorganic ions determined on the HT surface indicates more efficient film formation which can be attributed to the preferential alloy microstructure.

4. Conclusions

In this study, a micro-alloyed Mg-Ca-Zn alloy containing the contaminants was analyzed. Following the alloy preparation, the equal-channel angular pressing (ECAP) process was employed to refine the grain structure, thereby enhancing the mechanical properties and improving resistance to pitting corrosion. Various characterization techniques were utilized to investigate the effects of grain refinement on the overall behavior of the alloy. Based on these investigations, the following conclusions have been drawn:

(1) After ECAP processing, the microstructure undergoes significant refinement, producing a finer, more homogeneously distributed equiaxed grain structure compared to the heat-treated alloy.
(2) The alloy demonstrates increased ultimate tensile strength and yield strength after the four-pass ECAP process, while elongation remains relatively unchanged before and after processing. This shows that tensile strength is significantly influenced by grain size, whereas elongation at fracture shows minimal dependence on it, which is attributable to the stronger change in texture.
(3) The presence of Si leads to the formation of the MgCaSi phase, which positively influences the overall corrosion resistance, along with the $Ca_2Mg_6Zn_3$ phase. Electrochemical results further indicate that the overall corrosion resistance of the heat-treated alloy is slightly better than that of the ECAP-processed alloy; however, the ECAP-processed alloy exhibits significantly greater resistance to pitting corrosion compared to the heat-treated alloy.
(4) XPS analysis further confirms the formation of stable and coherent protective oxide layers on both surfaces.

Therefore, the enhancement in mechanical properties and pitting corrosion resistance has been achieved more efficiently and cost-effectively in the Mg-Ca-Zn alloy through grain refinement. This work demonstrates a cost-effective method for preparing micro-alloyed magnesium alloys with superior mechanical performance and improved pitting corrosion resistance, paving the way for next-generation lightweight materials that can enhance mechanical performance and improve clinical outcomes for patients.

Declaration of competing interest

The authors declare that they have no known competing financial interests or personal relationships that could have appeared to influence the work reported in this paper.

Acknowledgement

We sincerely appreciate the support provided by the National Science Center, Poland (grant no. 2024/53/B/ST11/00799). We gratefully acknowledge Polish high-performance computing infrastructure PLGrid (HPC Center: ACK Cyfronet AGH) for providing computer facilities and support within computational grant no. PLG/2025/018876.

Appendix A. Supplementary data

Supplementary data to this article can be found online at https://doi.org/10.1016/j.jmrt.2026.04.025.

Data availability

Research data will be made available on request.

References

[1] Liu F, Chen C, Niu J, Pei J, Zhang H, Huang H, Yuan G. The processing of Mg alloy micro-tubes for biodegradable vascular stents. Mater Sci Eng C 2015;48:400–7. https://doi.org/10.1016/j.msec.2014.12.024.
[2] Li M, Jiang M, Gao Y, Zheng Y, Liu Z, Zhou C, Huang T, Gu X, Li A, Fang J, Ji X. Current status and outlook of biodegradable metals in neuroscience and their potential applications as cerebral vascular stent materials. Bioact Mater 2022;11:140–53. https://doi.org/10.1016/j.bioactmat.2021.09.025.
[3] Staiger MP, Pietak AM, Huadmai J, Dias G. Magnesium and its alloys as orthopedic biomaterials: a review. Biomaterials 2006;27:1728–34. https://doi.org/10.1016/j.biomaterials.2005.10.003.
[4] Cheon K-H, Park C, Kang M-H, Park S, Kim J, Jeong S-H, Kim H-E, Jung H-D, Jang T-S. A combination strategy of functionalized polymer coating with Ta ion implantation for multifunctional and biodegradable vascular stents. J Magnesium Alloys 2021;9:2194–206. https://doi.org/10.1016/j.jma.2021.07.019.
[5] Li Y, Wang Y, Shen Z, Miao F, Wang J, Sun Y, Zhu S, Zheng Y, Guan S. A biodegradable magnesium alloy vascular stent structure: design, optimisation and evaluation. Acta Biomater 2022;142:402–12. https://doi.org/10.1016/j.actbio.2022.01.045.
[6] Shu C, He H, Fan B, Li J, Wang T, Li D, Li Y, He H. Biocompatibility of vascular stents manufactured using metal injection molding in animal experiments. Trans Nonferrous Met Soc China 2022;32:569–80. https://doi.org/10.1016/s1003-6326(22)65816-3.
[7] Chen Y, Xu Z, Smith C, Sankar J. Recent advances on the development of magnesium alloys for biodegradable implants. Acta Biomater 2014;10:4561–73. https://doi.org/10.1016/j.actbio.2014.07.005.
[8] Akbarzadeh FZ, Sarraf M, Ghomi ER, Kumar VV, Salehi M, Ramakrishna S, Bae S. A state-of-the-art review on recent advances in the fabrication and characteristics of magnesium-based alloys in biomedical applications. J Magnesium Alloys 2024;12:2569–94. https://doi.org/10.1016/j.jma.2024.06.015.
[9] Wiese A, Pape HC. Bone defects caused by high-energy injuries, bone loss, infected nonunions, and nonunions. Orthop Clin N Am 2010;41:1–4. https://doi.org/10.1016/j.ocl.2009.07.003.
[10] Goldberg VM, Buckwalter JA, Hayes WC, Koval KJ. Orthopaedic challenges in an aging population. Instr Course Lect 1997;46:417–22.
[11] Yan LD, Sufra R, St Sauveur R, Jean-Pierre MC, Apollon A, Malebranche R, Théard M, Pierre G, Dévieux J, Lau J, Mourra N, Roberts NLS, Rasul R, Nash D, Pirmohamed AM, Devereux RB, Lee MH, Kwan GF, Safford MM, Adrien L, Alfred JP, Deschamps M, Severe P, Fitzgerald DW, Pape JW, Rouzier V, McNairy ML, Yan LD, Sufra R, St Sauveur R, Jean-Pierre MC, Pierre JL, Apollon A, Malebranche R, Théard M, Pierre G, Dévieux J, Lau J, Mourra N, Metz M, Smith C, Sabwa S, Clermont A, Roberts NLS, Rasul R, Nash D, Pirmohamed AM, Devereux RB, Lee MH, Kwan GF, Safford M, Adrien L, Alfred JP, Deschamps M,

Severe P, Fitzgerald DW, Pape JW, Rouzier V, McNairy ML. Spectrum of prevalent cardiovascular diseases in urban Port-au-Prince, Haiti: a population-based cross-sectional study. Lancet Reg Health, Am 2024;33:100729. https://doi.org/10.1016/j.lana.2024.100729.
[12] Nasr Azadani M, Zahedi A, Bowoto OK, Oladapo BI. A review of current challenges and prospects of magnesium and its alloy for bone implant applications. Prog Biomater 2022;11:1–26. https://doi.org/10.1007/s40204-022-00182-x.
[13] Chu JH, Tong LB, Jiang ZH, Zou DN, Wang QJ, Liu SF, Zhang HJ. A comparison study of Ce/La and ca microalloying on the bio-corrosion behaviors of extruded Mg-Zn alloys. J Magnesium Alloys 2020;8:1269–80. https://doi.org/10.1016/j.jma.2019.09.011.
[14] Chen F, Wang J, Cheng Y, Li R, Wang Y, Chen Y, Scott T, Tucker KL. Magnesium and cognitive health in adults: a systematic review and meta-analysis. Adv Nutr 2024;15:100272. https://doi.org/10.1016/j.advnut.2024.100272.
[15] Mathew Abraham A, Subramani V. Effect of magnesium as biomaterial in biodegrdation. Mater Today Proc 2023. https://doi.org/10.1016/j.matpr.2023.05.424.
[16] Bahrampour S, Bordbar-Khiabani A, Siadati MH, Gasik M. Tuning biomechanical behavior and biocompatibility of mg–zn–ca alloys by Mn3O4 incorporated plasma electrolytic oxidation coatings. Ceram Int 2024;50:29703–10. https://doi.org/10.1016/j.ceramint.2024.05.267.
[17] Sun L, Dong N, Wang J, Ma H, Jin P, Peng Y. Effect of solid solution Zn atoms on corrosion behaviors of Mg-2Nd-2Zn alloys. Corros Sci 2022;196:110023. https://doi.org/10.1016/j.corsci.2021.110023.
[18] Xu X, Li W, Wan B, Jin S, Chen K, Su F. Extremely improved the corrosion resistance and anti-wear behavior of aluminum alloy in 3.5% NaCl solution via amorphous CrAlN coating protection. Corros Sci 2024;230:111952. https://doi.org/10.1016/j.corsci.2024.111952.
[19] Zhang Y, Yang H, Huang R, Sun P, Zheng S, Li M, Wang X, Du Q. Investigation of microstructure and corrosion resistance of an Al-Zn-Mg-Cu alloy under various ageing conditions. Corros Sci 2024;227:111719. https://doi.org/10.1016/j.corsci.2023.111719.
[20] Liu X, Huang Q, Zhang C, Dai Y, Tang K, Zhang D, Qi F, Wu Y, Ouyang X. Fe modified Ca-Mg-P coating with synergistic antibacterial, photothermal and osteogenic properties on magnesium alloys. J Magnesium Alloys 2026;15:101921. https://doi.org/10.1016/j.jma.2025.09.036.
[21] He T, Liu X, Xiao Z, Dai Y, Dou Y, She J, Lu L, Yang Y, Wang L, Zhao N, Wei W, Qi F, Ouyang X. The mechanisms of varying doses of metal ion implantation (Ag, Ti and Zr) on microstructure and properties of pure magnesium. Rare Met 2025;44:6730–47. https://doi.org/10.1007/s12598-025-03354-3.
[22] Liu X, Xiao Z, Yuan Y, Huang Q, Tang K, Dai Y, Zhang D, She J, Peng F, Qi F, Ouyang X. Corrosion-resistant and bioactive FeMn-CaP-Col@CS coating on magnesium alloy for orthopedic implants: fabrication and characterization. Metals Advances 2026;39:1–12. https://doi.org/10.1016/j.metadv.2025.12.004.
[23] Li L, Zhang Z, Zhang D, Qi F, Dai Y, Wei W, Ouyang X. Effects of metal ion implantation (Fe, Ti, Zn and Zr) on mechanical properties, corrosion resistance and biocompatibility of WE43 Mg alloy. J Magnesium Alloys 2025;13:296–310. https://doi.org/10.1016/j.jma.2024.05.005.
[24] Xu L, Yamamoto A. Characteristics and cytocompatibility of biodegradable polymer film on magnesium by spin coating. Colloids Surf B Biointerfaces 2012;93:67–74. https://doi.org/10.1016/j.colsurfb.2011.12.009.
[25] Wei L, Gao Z. Recent research advances on corrosion mechanism and protection, and novel coating materials of magnesium alloys: a review. RSC Adv 2023;13:8427–63. https://doi.org/10.1039/d2ra07829e.
[26] Esmaily M, Svensson JE, Fajardo S, Birbilis N, Frankel GS, Virtanen S, Arrabal R, Thomas S, Johansson LG. Fundamentals and advances in magnesium alloy corrosion. Prog Mater Sci 2017;89:92–193. https://doi.org/10.1016/j.pmatsci.2017.04.011.
[27] Li JN, Cao P, Zhang XN, Zhang SX, He YH. In vitro degradation and cell attachment of a PLGA coated biodegradable Mg–6Zn based alloy. J Mater Sci 2010;45:6038–45. https://doi.org/10.1007/s10853-010-4688-9.
[28] Qin X, Liu H, Chen Y, Yuan Z, Sun C, Wu Y, Yan K, Ju J, Jiang J, Bai J. Optimization in strength-ductility of Mg-Gd-Y-Zn-Al alloy through microstructural heredity process regulation. Mater Sci Eng, A 2025;944:148930. https://doi.org/10.1016/j.msea.2025.148930.
[29] Chen Y, Liu H, Qin X, Yuan Z, Sun C, Wu Y, Yan K, Ju J, Jiang J, Bai J. Achieving strength-ductility synergy in Mg-Gd-Y-Zn-Al alloy via toughening effect of nano-sized W-Mg3RE2Zn3 phases within LPSO structures. Scr Mater 2026;270:116938. https://doi.org/10.1016/j.scriptamat.2025.116938.
[30] Zengin H, Krawiec H, Minarik P, Hassel AW. Influence of secondary phases and their redistribution by deformation on corrosion behaviour of magnesium alloys – a short review. J Mater Res Technol 2025;37:122–32. https://doi.org/10.1016/j.jmrt.2025.06.022.
[31] Aksenov D, Nazarov A, Shishkunova M, Asfandiyarov R, Raab A, Sementeeva Y. Bulk ultrasonic treatment of magnesium and Mg-Zn-Zr alloy subjected to ECAP. J Alloys Compd 2025;1014:178632. https://doi.org/10.1016/j.jallcom.2025.178632.
[32] Orlov D, Ralston KD, Birbilis N, Estrin Y. Enhanced corrosion resistance of Mg alloy ZK60 after processing by integrated extrusion and equal channel angular pressing. Acta Mater 2011;59:6176–86. https://doi.org/10.1016/j.actamat.2011.06.033.
[33] Zeng R, Kainer KU, Blawert C, Dietzel W. Corrosion of an extruded magnesium alloy ZK60 component—The role of microstructural features. J Alloys Compd 2011;509:4462–9. https://doi.org/10.1016/j.jallcom.2011.01.116.
[34] Li J, Qiu Y, Yang J, Sheng Y, Yi Y, Zeng X, Chen L, Yin F, Su J, Zhang T, Tong X, Guo B. Effect of grain refinement induced by wire and arc additive manufacture (WAAM) on the corrosion behaviors of AZ31 magnesium alloy in NaCl solution. J Magnesium Alloys 2023;11:217–29. https://doi.org/10.1016/j.jma.2021.04.007.
[35] He S, Wang C, Sun C, Zhang Y, Yan K, Jiang J, Bai J, Xue F, Liu H. Corrosion properties of ECAP-processed Mg−Al−Ca−Mn alloys with separate Al2Ca and Mg2Ca phases. Trans Nonferrous Met Soc China 2022;32:2527–40. https://doi.org/10.1016/S1003-6326(22)65963-6.
[36] Rzepa S, Trojanová Z, Džugan J, Valiev RZ, Koukolíková M, Melzer D, Brázda M. Effect of ECAP processing on microstructure and mechanical behaviour of Ti-6Al-4V manufactured by directed energy deposition. Mater Char 2023;196:112622. https://doi.org/10.1016/j.matchar.2022.112622.
[37] Choi HY, Kim WJ. Effect of thermal treatment on the bio-corrosion and mechanical properties of ultrafine-grained ZK60 magnesium alloy. J Mech Behav Biomed Mater 2015;51:291–301. https://doi.org/10.1016/j.jmbbm.2015.07.019.
[38] Parfenov EV, Kulyasova OB, Mukaeva VR, Mingo B, Farrakhov RG, Cherneikina YaV, Yerokhin A, Zheng YF, Valiev RZ. Influence of ultra-fine grain structure on corrosion behaviour of biodegradable Mg-1Ca alloy. Corros Sci 2020;163:108303. https://doi.org/10.1016/j.corsci.2019.108303.
[39] Tang J, Chen L, Li Z, Zhao G, Zhang C. Formation of abnormal coarse grains and its effects on corrosion behaviors of solution treated ZK60 Mg alloy. Corros Sci 2021;180:109201. https://doi.org/10.1016/j.corsci.2020.109201.
[40] Pei QX, Hu BH, Lu C, Wang YY. A finite element study of the temperature rise during equal channel angular pressing. Scr Mater 2003;49:303–8. https://doi.org/10.1016/S1359-6462(03)00284-7.
[41] Jivan R, Eskandarzade M, Bewsher S, Leighton M, Mohammadpour M, Saremi-Yarahmadi S. Application of solid lubricant for enhanced frictional efficiency of deep drawing process. Proc IME C J Mech Eng Sci 2022;236:624–34. https://doi.org/10.1177/0954406221994886.
[42] Mesmer G, Colton J. Variation of the friction conditions in cold ring compression tests of aluminum 1100-O and aluminum 6061-T6 as applied to room temperature forging in low- and middle-income countries. Cogent Eng 2024;11:2399961. https://doi.org/10.1080/23311916.2024.2399961.
[43] Khalilpourazary S, Alimirzaloo V, Karami Goodarzi S, Hosseinpour G. The effect of equal channel angular pressing on friction coefficients of copper samples in the ring-compression test. J Materi Eng and Perform 2022;31:3835–46. https://doi.org/10.1007/s11665-021-06465-x.
[44] Daghigh M, Mohri M, Nili-ahmadabadi M. Tailoring deformation homogeneity of WE43 alloy through strain rate sensitivity and back pressure during equal channel angular pressing. J Materi Eng and Perform 2024;33:12604–19. https://doi.org/10.1007/s11665-024-09970-x.
[45] Su Y, Lin J, Su Y, Zai W, Li G, Wen C. Investigation on composition, mechanical properties, and corrosion resistance of Mg-0.5Ca-X(Sr, Zr, Sn) biological alloy. Scanning 2018;2018:6519310. https://doi.org/10.1155/2018/6519310.
[46] Nazri NA, Sani MSM, Mansor MN, Zahari SN. Model updating of friction stir welding for aluminium and magnesium plate structure. MATEC Web of Conferences 2018;150:04004. https://doi.org/10.1051/matecconf/201815004004.
[47] Zander D, Zumdick NA. Influence of Ca and Zn on the microstructure and corrosion of biodegradable Mg–Ca–Zn alloys. Corros Sci 2015;93:222–33. https://doi.org/10.1016/j.corsci.2015.01.027.
[48] Sun Y, Zhang B, Wang Y, Geng L, Jiao X. Preparation and characterization of a new biomedical Mg–Zn–Ca alloy. Mater Des 2012;34:58–64. https://doi.org/10.1016/j.matdes.2011.07.058.
[49] Bakhsheshi-Rad HR, Abdul-Kadir MR, Idris MH, Farahany S. Relationship between the corrosion behavior and the thermal characteristics and microstructure of Mg–0.5Ca–xZn alloys. Corros Sci 2012;64:184–97. https://doi.org/10.1016/j.corsci.2012.07.015.
[50] Gao JC, Wu S, Wang Y, Qiao LY. Study on corrosion and degradation behavior of Mg-Ca alloy in simulated body fluid. MSF 2009;610–613:942–5. https://doi.org/10.4028/www.scientific.net/msf.610-613.942.
[51] Jin Y, Blawert C, Feyerabend F, Bohlen J, Silva Campos M, Gavras S, Wiese B, Mei D, Deng M, Yang H, Willumeit-Römer R. Time-sequential corrosion behaviour observation of micro-alloyed Mg-0.5Zn-0.2Ca alloy via a quasi-in situ approach. Corros Sci 2019;158:108096. https://doi.org/10.1016/j.corsci.2019.108096.
[52] Liu C, Chen X, Chen J, Atrens A, Pan F. The effects of Ca and Mn on the microstructure, texture and mechanical properties of Mg-4 Zn alloy. J Magnesium Alloys 2021;9:1084–97. https://doi.org/10.1016/j.jma.2020.03.012.
[53] Bazhenov VE, Li AV, Komissarov AA, Koltygin AV, Tavolzhanskii SA, Bautin VA, Voropaeva OO, Mukhametshina AM, Tokar AA. Microstructure and mechanical and corrosion properties of hot-extruded Mg–Zn–Ca–(Mn) biodegradable alloys. J Magnesium Alloys 2021;9:1428–42. https://doi.org/10.1016/j.jma.2020.11.008.
[54] Gan WM, Wu K, Zheng MY, Wang XJ, Chang H, Brokmeier H-G. Microstructure and mechanical property of the ECAPed Mg2Si/Mg composite. Mater Sci Eng, A 2009;516:283–9. https://doi.org/10.1016/j.msea.2009.03.034.
[55] Yeh C-L, Chen K-T. Synthesis of FeSi-Al2O3 composites by autowave combustion with metallothermic reduction. Metals 2021;11:258. https://doi.org/10.3390/met11020258.
[56] Brutti S, Ciccioli A, Balducci G, Gigli G, Manfrinetti P, Napoletano M. Thermodynamic stabilities of intermediate phases in the Ca–Si system. J Alloys Compd 2001;317–318:525–31. https://doi.org/10.1016/S0925-8388(00)01381-5.
[57] Wu J, Chong X, Jiang Y, Feng J. Stability, electronic structure, mechanical and thermodynamic properties of Fe-Si binary compounds. J Alloys Compd 2017;693:859–70. https://doi.org/10.1016/j.jallcom.2016.09.225.
[58] Wu R, Wang Y-P, Yang Y, Luo D-M, Meng H, Ma L, Tang B-Y. Structural and mechanical properties of ternary MgCaSi phase: a study by density functional theory. J Chem Res 2020;44:50–9. https://doi.org/10.1177/1747519819885479.

[59] Wu R, Wang Y-P, Shao L, Wang W, Tang B-Y. Thermodynamic property of ternary compound MgCaSi: a study from ab initio Debye-Grüneisen model. Chin J Chem Eng 2021;40:315–22. https://doi.org/10.1016/j.cjche.2020.11.033.
[60] Carbonneau Y, Couture A, Van Neste A, Tremblay R. On the observation of a new ternary MgSiCa phase in Mg-Si alloys. Metall Mater Trans A 1998;29:1759–63. https://doi.org/10.1007/s11661-998-0099-9.
[61] Minárik P, Král R, Čížek J, Chmelík F. Effect of different *c/a* ratio on the microstructure and mechanical properties in magnesium alloys processed by ECAP. Acta Mater 2016;107:83–95. https://doi.org/10.1016/j.actamat.2015.12.050.
[62] Shi DF, Ma A, Pérez-Prado MT, Cepeda-Jiménez CM. Activation of second-order pyramidal slip and other secondary mechanisms in solid solution Mg-Zn alloys and their effect on tensile ductility. Acta Mater 2023;244:118555. https://doi.org/10.1016/j.actamat.2022.118555.
[63] Cepeda-Jiménez CM, Molina-Aldareguia JM, Pérez-Prado MT. Origin of the twinning to slip transition with grain size refinement, with decreasing strain rate and with increasing temperature in magnesium. Acta Mater 2015;88:232–44. https://doi.org/10.1016/j.actamat.2015.01.032.
[64] Yu Y, Wei Y, Song Y, Shou H, He L. Mechanisms of temperature effects on the tensile properties and dislocation behavior of Mg-Zn-Ca alloys. Sci Rep 2025;15:18066. https://doi.org/10.1038/s41598-025-01805-6.
[65] Suh B-C, Kim JH, Hwang JH, Shim M-S, Kim NJ. Twinning-mediated formability in Mg alloys. Sci Rep 2016;6:22364. https://doi.org/10.1038/srep22364.
[66] Iwahashi Y, Horita Z, Nemoto M, Langdon TG. The process of grain refinement in equal-channel angular pressing. Acta Mater 1998;46:3317–31. https://doi.org/10.1016/s1359-6454(97)00494-1.
[67] Segal VM. Materials processing by simple shear. Mater Sci Eng, A 1995;197:157–64. https://doi.org/10.1016/0921-5093(95)09705-8.
[68] Xu W, Yu J, Jia L, Gao C, Miao Z, Wu G, Li G, Zhang Z. Grain refinement impact on the mechanical properties and wear behavior of Mg-9Gd-3Y-2Zn-0.5Zr alloy after decreasing temperature reciprocating upsetting-extrusion. J Magnesium Alloys 2022;10:3506–19. https://doi.org/10.1016/j.jma.2021.03.021.
[69] Martynenko N, Lukyanova E, Serebryany V, Prosvirnin D, Terentiev V, Raab G, Dobatkin S, Estrin Y. Effect of equal channel angular pressing on structure, texture, mechanical and in-service properties of a biodegradable magnesium alloy. Mater Lett 2019;238:218–21. https://doi.org/10.1016/j.matlet.2018.12.024.
[70] Lentz M, Behringer A, Fahrenson C, Beyerlein IJ, Reimers W. Grain size effects on primary, secondary, and tertiary twin development in Mg-4 wt pct Li (-1 wt pct Al) alloys. Metall Mater Trans A 2014;45:4737–41. https://doi.org/10.1007/s11661-014-2491-y.
[71] Vaughan MW, Nasim W, Dogan E, Herrington JS, Proust G, Benzerga AA, Karaman I. Interplay between the effects of deformation mechanisms and dynamic recrystallization on the failure of Mg-3Al-1Zn. Acta Mater 2019;168:448–72. https://doi.org/10.1016/j.actamat.2019.02.010.
[72] Barnett MR, Stanford N, Cizek P, Beer A, Xuebin Z, Keshavarz Z. Deformation mechanisms in Mg alloys and the challenge of extending room-temperature plasticity. JOM 2009;61:19–24. https://doi.org/10.1007/s11837-009-0115-6.
[73] Dogan E, Vaughan MW, Wang SJ, Karaman I, Proust G. Role of starting texture and deformation modes on low-temperature shear formability and shear localization of Mg–3Al–1Zn alloy. Acta Mater 2015;89:408–22. https://doi.org/10.1016/j.actamat.2014.12.006.
[74] Rodriguez AK, Ayoub GA, Mansoor B, Benzerga AA. Effect of strain rate and temperature on fracture of magnesium alloy AZ31B. Acta Mater 2016;112:194–208. https://doi.org/10.1016/j.actamat.2016.03.061.
[75] Dogan E, Karaman I, Ayoub G, Kridli G. Reduction in tension–compression asymmetry via grain refinement and texture design in Mg–3Al–1Zn sheets. Mater Sci Eng, A 2014;610:220–7. https://doi.org/10.1016/j.msea.2014.04.112.
[76] Sanusi KO, Makinde OD, Oliver GJ. Equal channel angular pressing technique for the formation of ultra-fine grained structures. South Afr J Sci 2012;108. https://doi.org/10.4102/sajs.v108i9/10.212.
[77] Drozdenko D, Fekete K, Dobroň P, Knapek M, Máthis K, Minárik P, Yamasaki M, Kawamura Y. The yield point phenomenon in ultrafine-grained dilute Mg-Zn-Y alloys. Mater Lett 2023;330:133315. https://doi.org/10.1016/j.matlet.2022.133315.
[78] Horky J, Bryła K, Krystian M, Mozdzen G, Mingler B, Sajti L. Improving mechanical properties of lean Mg–Zn–Ca alloy for absorbable implants via double equal channel angular pressing (D-ECAP). Mater Sci Eng, A 2021;826:142002. https://doi.org/10.1016/j.msea.2021.142002.
[79] Lelek-Borkowska U, Wróbel M, Marzec M, Kustra P, Milenin A. Mg–Ca surgical wires degradation in animal serum. Metall Mater Trans A 2024;55:2141–52. https://doi.org/10.1007/s11661-024-07387-8.
[80] Ren L, Liu X, Cao H, Tang Y, Qi F, Zhao N, Dai Y, Ouyang X. Mechanical and corrosion properties of hydrogen-free DLC coatings prepared on degradable as-extruded WE43 alloy using FCVA technology. Surf Coating Technol 2024;476:130293. https://doi.org/10.1016/j.surfcoat.2023.130293.
[81] Jamesh M, Kumar S, Sankara Narayanan TSN. Corrosion behavior of commercially pure Mg and ZM21 Mg alloy in Ringer's solution – long term evaluation by EIS. Corros Sci 2011;53:645–54. https://doi.org/10.1016/j.corsci.2010.10.011.
[82] Święch D, Palumbo G, Jabłoński P, Gajewska M, Golda A, Koziel J, Mingo B, Piergies N, Engelberg DL. Titanium coated with gold nanoparticles: a multifaceted investigation through electrochemical, spectroscopic, and biological approaches. Appl Surf Sci 2025;711:164032. https://doi.org/10.1016/j.apsusc.2025.164032.
[83] Xiao Z, Ren L, Guo C, Liang L, Dai Y, Tang K, Lu L, Qi F, She J, Wang L, Ouyang X. Enhanced corrosion resistance, mechanical properties, and biocompatibility of N-DLC coatings prepared on WE43 alloy via FCVA technology. J Alloys Compd 2025;1010:178106. https://doi.org/10.1016/j.jallcom.2024.178106.
[84] Xu W, Wu Y, Snihirova D, Wang L, Deng M, Wang C, Lamaka SV, Zheludkevich ML, Höche D. Mathematical modeling of salicylate effects on high-purity Mg anode for aqueous primary Mg-Air batteries. J Magnesium Alloys 2025;13:1506–22. https://doi.org/10.1016/j.jma.2025.02.027.
[85] Hashemi M, Alizadeh R, Aashuri H. Hydrothermally coated Mg–1Zn–0.2Ag alloy with improved mechanical and corrosion properties: a comparative study on the role of substrate. J Mater Sci 2024;59:16324–40. https://doi.org/10.1007/s10853-024-10157-x.
[86] Savaedi Z, Mirzadeh H, Aghdam RM, Mahmudi R. Effect of grain size on the mechanical properties and bio-corrosion resistance of pure magnesium. J Mater Res Technol 2022;19:3100–9. https://doi.org/10.1016/j.jmrt.2022.06.048.
[87] El-Garaihy WH, Alateyah AI, Ahmed MMZ, El-Asfoury MS, Alawad MO, BaQais A, Zedan Y, Salem HG. Improving In-Vitro corrosion and degradation performance of mg–zn–ca alloy for biomedical applications by equal channel angular pressing. Met Mater Int 2024;30:1701–21. https://doi.org/10.1007/s12540-023-01599-0.
[88] Palumbo G, Thorpe SJ, Aust KT. On the contribution of triple junctions to the structure and properties of nanocrystalline materials. Scripta Metall Mater 1990;24:1347–50. https://doi.org/10.1016/0956-716X(90)90354-J.
[89] Zeller-Plumhoff B, Gile M, Priebe M, Slominska H, Boll B, Wiese B, Würger T, Willumeit-Römer R, Meißner RH. Exploring key ionic interactions for magnesium degradation in simulated body fluid – a data-driven approach. Corros Sci 2021;182:109272. https://doi.org/10.1016/j.corsci.2021.109272.
[90] Du H, Wei Z, Liu X, Zhang E. Effects of Zn on the microstructure, mechanical property and bio-corrosion property of Mg–3Ca alloys for biomedical application. Mater Chem Phys 2011;125:568–75. https://doi.org/10.1016/j.matchemphys.2010.10.015.
[91] Jin Y, Blawert C, Yang H, Wiese B, Feyerabend F, Bohlen J, Mei D, Deng M, Campos MS, Scharnagl N, Strecker K, Bode J, Vogt C, Willumeit-Römer R. Microstructure-corrosion behaviour relationship of micro-alloyed Mg-0.5Zn alloy with the addition of Ca, Sr, Ag, In and Cu. Mater Des 2020;195:108980. https://doi.org/10.1016/j.matdes.2020.108980.
[92] Xu Y, Li J, Qi M, Guo W, Deng Y. A newly developed Mg-Zn-Gd-Mn-Sr alloy for degradable implant applications: influence of extrusion temperature on microstructure, mechanical properties and in vitro corrosion behavior. Mater Char 2022;188:111867. https://doi.org/10.1016/j.matchar.2022.111867.
[93] Xu L, Zhang E, Yin D, Zeng S, Yang K. In vitro corrosion behaviour of Mg alloys in a phosphate buffered solution for bone implant application. J Mater Sci Mater Med 2008;19:1017–25. https://doi.org/10.1007/s10856-007-3219-y.
[94] Cesarz-Andraczke K, Nowosielski R. Surface structure and corrosion behavior of Mg68−xZn28+xCa4(x = 0.4) bulk metallic glasses after immersion in Ringer's solution. J Materi Eng and Perform 2019;28:2365–77. https://doi.org/10.1007/s11665-019-04001-6.
[95] High Resolution XPS of Organic Polymers: The Scienta ESCA300 Database, Beamson G, Briggs D. J Chem Educ 1993;70:A25. https://doi.org/10.1021/ed070pA25.5.
[96] Rouxhet PG, Genet MJ. XPS analysis of bio-organic systems. Surf Interface Anal 2011;43:1453–70. https://doi.org/10.1002/sia.3831.
[97] Naumkin AV, Kraut-Vass A, Gaarenstroom SW, Powell CJ. NIST X-ray photoelectron spectroscopy database. Gaithersburg: National Institute of Standards and Technology; 2012., version 4.1. https://scholar.google.com/scholar?cluster=8075639019446164872&hl=en&oi=scholarr. [Accessed 24 August 2025].
[98] Skaanvik SA, Henderson JD, Noël JJ, Biesinger MC. Speciation of magnesium surfaces by X-ray photoelectron spectroscopy (XPS). Surf Interface Anal 2025;57:717–28. https://doi.org/10.1002/sia.70003.
[99] Nam ND. Role of zinc in enhancing the corrosion resistance of Mg-5Ca alloys. J Electrochem Soc 2016;163:C76–84. https://doi.org/10.1149/2.0281603jes.